## RESEARCH

# Hydraulic behavior of fault zones in pump tests of geothermal wells: a parametric analysis using numerical simulations for the Upper Jurassic aquifer of the North Alpine Foreland Basin

Florian Konrad[1] , Alexandros Savvatis[2], Florian Wellmann[3] and Kai Zosseder[1]*

*Correspondence:
kai.zosseder@tum.de
[1] Technical University Munich,
Arcisstraße 21, 80333 Munich,
Germany
Full list of author information
is available at the end of the
article

## Abstract

Fault zones in the Upper Jurassic aquifer of the North Alpine Foreland Basin are generally regions with possibly increased hydraulic properties. They are consequently often part of the geothermal exploration concepts in this area and a primary target for the drilling operation. Data from this aquifer, gathered in pump tests, however, show that only four out of 41 successful wells exhibit hydraulic proof for the presence of such a fault zone in terms of a bi-/linear flow regime. Besides technical effects, also the contrast in hydraulic properties itself, between fault zone and surrounding host rock, can prevent the detection of a fault zone in pump test data. This means a certain threshold has to be surpassed until its effects become clearly visible. A simplified realistic numerical model was constructed and calibrated with pressure data from an exploration site in the south of Munich. This model was then used to observe the presence of linear and bilinear flows in dependence on the Malm aquifers parameter space. Sampling the possible hydraulic property combinations with the help of an HPC (high-performance computing) cluster and automating the detection of the corresponding main flow type allowed to quantify the areas in parameter space where the fault zone-related flow regimes of interest are present. Through the investigation of more than 30,000 combinations between fault zone permeability, matrix permeability, fault zone storage, matrix storage and fault zone thickness, it was found that, in the parameter space of the Malm aquifer, a bilinear flow can be observed for the first time only if the matrix permeability is lower than $2.0 \times 10^{-13}$ $m^2$, and a linear flow for matrix permeability values below $6.0 \times 10^{-14}$ $m^2$. Additionally, it was shown that fault zones, which have better hydraulic properties than the surrounding matrix, can indeed be hidden in pumping tests due to the parameter setting.

**Keywords:** Numerical simulation, Geothermal energy, Well test analysis, Parametric study, Fault zone, Malm, Molasse Basin

Konrad *et al. Geotherm Energy* (2019) 7:25

Page 2 of 28

## Introduction

One of the most important aquifers for deep geothermal energy exploration in Europe is located in southern Germany in the North Alpine Foreland Basin. Carbonatic rocks of the Upper Jurassic form a mid-enthalpy karstified and fractured porous reservoir. They can be up to 600 m thick and mainly consist of small-pored white limestones as well as fine- to coarse-grained dolomites (Agemar et al. 2014; Mraz 2019; Wolfgramm et al. 2007). These reservoir rocks compose the ground surface at the northern border of the foreland basin (Frankish and Swabian Alb) and are inclined to the south due to lithospheric bending caused by the Alpine orogenesis. It is this flexural bending that caused the development of normal faults parallel to the Alps throughout the entire foreland basin also crossing the Upper Jurassic aquifer (Cacace et al. 2013; Fritzer 2012). Close to the alpine range, this reservoir can therefore be found again only in a depth of 5000 m or more (Böhm et al. 2013). The inclination, and consequently the possibility for high temperatures together with favorable hydraulic properties, potentially high-permeable fault zones and karstification, are the reason for the importance of the Upper Jurassic aquifer (also called Malm aquifer) in the context of geothermal energy exploration (Agemar et al. 2014; Birner 2013).

The majority of geothermal plants that tap into the Upper Jurassic aquifer are located in the area of Munich (Germany), where a high energy demand and the aquifer's best hydraulic properties coincide. Hydrothermal doublets with an installed thermal output of approximately 235 MWt and 26 MWe installed electric output access the energy stored in the subsurface (Agemar et al. 2014). Currently 44 completed wells in total can be found here. (Three of them are unsuccessful, status June 2019.) In addition, several new explorations sites are already in development.

After the construction of such a new geothermal well is finished, a next step is to assess its productivity and the resulting profitability. For this purpose, a long-term pumping test gets deployed right after a short cleaning-through-acidification period. (No other stimulation treatments are applied for deep geothermal wells in the North Alpine Foreland Basin.) The goal of this test is to measure the pressure drawdown until a quasi-stabilization is reached followed by a shut-in and the observation of the pressure build-up. This data set is subsequently evaluated by the use of pressure transient analysis (PTA) with its key tool, the Bourdet derivative (DER) (Bourdet 2002). The reservoir performance (PI value) as well as the hydraulic properties at the corresponding drilling site is thus identified. Additionally, the quality of communication between well and reservoir is determined, and an understanding of the aquifers flow behavior is obtained (Bourdet 2002). By putting those findings into a spatial context, future exploration strategies can be developed and improved (Savvatis 2012).

Fault zones are of high importance for designing such exploration concepts (Böhm et al. 2012). To quantify the hydraulic influence of a fault zone for the productivity of a well, detailed knowledge about geometry and hydraulic rock properties is essential but rarely available (Caine et al. 1996). By developing a deep understanding about the genesis of fault zones as well as the surrounding host rock and combining it with field investigations and laboratory measurements, the possibilities of their hydraulic behavior can be confined. But there are multiple additional local factors (e.g. stress field, actual tectonic history, rock facies and properties) which are difficult to

determine precisely, but which have a high influence on the faults hydraulic effect. A fully developed fault zone can generally be divided in two major elements: a fault core (the surface of major slip, consisting of low-permeability rocks) and the damage zone (intensively fractured host rock, consisting of high-permeable breccias). But depending on the previously mentioned factors these two elements can drastically vary in their hydraulic properties. Therefore, it is possible that fault zones, viewed as an integrative area from a hydraulic point of view, behave either transparent to fluid flow, as highly permeable conduits or as a barrier (Cacace et al. 2013; Caine et al. 1996; Micarelli et al. 2006; Michie et al. 2014; Moeck et al. 2015). Even though there is a high uncertainty involved in predicting this, for the exploration of the Upper Jurassic reservoir fault zones are generally thought of as an area with possibly increased hydraulic permeability and as an enhancement for the connection between well and aquifer (Böhm et al. 2013). They are consequently a key component for the majority of well concepts located in the South German Molasse Basin.

Field data from this area on the other hand show that 37 out of 41 geothermal wells portray a seemingly homogeneous flow behavior in their pumping tests (radial flow) (Savvatis 2012). This is contrary to the previously stated role of fault zones in applied exploration concepts. One would rather expect that many explorations sites detect a fault zone that is causing linear or bilinear flow. But in reality only four wells are known to show a fault zone-dominated flow behavior (Steiner et al. 2012; TUM 2019).

Hence, this study answers the question, which parameter settings are necessary to observe bilinear or linear flow behavior in a pumping test of the Upper Jurassic aquifer in southern Germany. It is also investigating whether the detection of fault zones in pumping tests can be masked due to a specific setting of the hydraulic properties in the fault zone and surrounding host rock. This knowledge is important for the evaluation of fault zones as viable targets in future exploration concepts. To achieve this, numerical simulations of pumping tests for a realistic aquifer geometry and a multitude of possible parameter settings with a representative and calibrated hydraulic model were carried out. It is the geometric freedom which gives the dedicated numerical modeling method an advantage over state-of-the-art commercial well test software solutions (e.g., Kappa, Fekete) which also have capabilities for parametric analysis but have a primary focus on analytical models (Houze et al. 2017; IHS 2016).

The simulated pumping tests were then analyzed with state-of-the-art pressure transient analysis methods in an automated fashion. The execution of the numerical simulations was done on an HPC (high-performance computing) system to ensure a sufficiently large number of simulated samples in the parameter space of the analyzed aquifer in a reasonable time while accounting for a realistic geometry. The resulting flow regimes were then identified, and their transition in parameter space was assessed. The presented approach is also valid beyond the investigated location and illustrates the combination of numerical simulations on a high-performance computer with well test analysis methodology to derive conclusions for hydraulic reservoir behavior observable in the field. Figure 1 presents an overview of the relevant theoretical flow regime types (left side) with their corresponding pressure curves, the
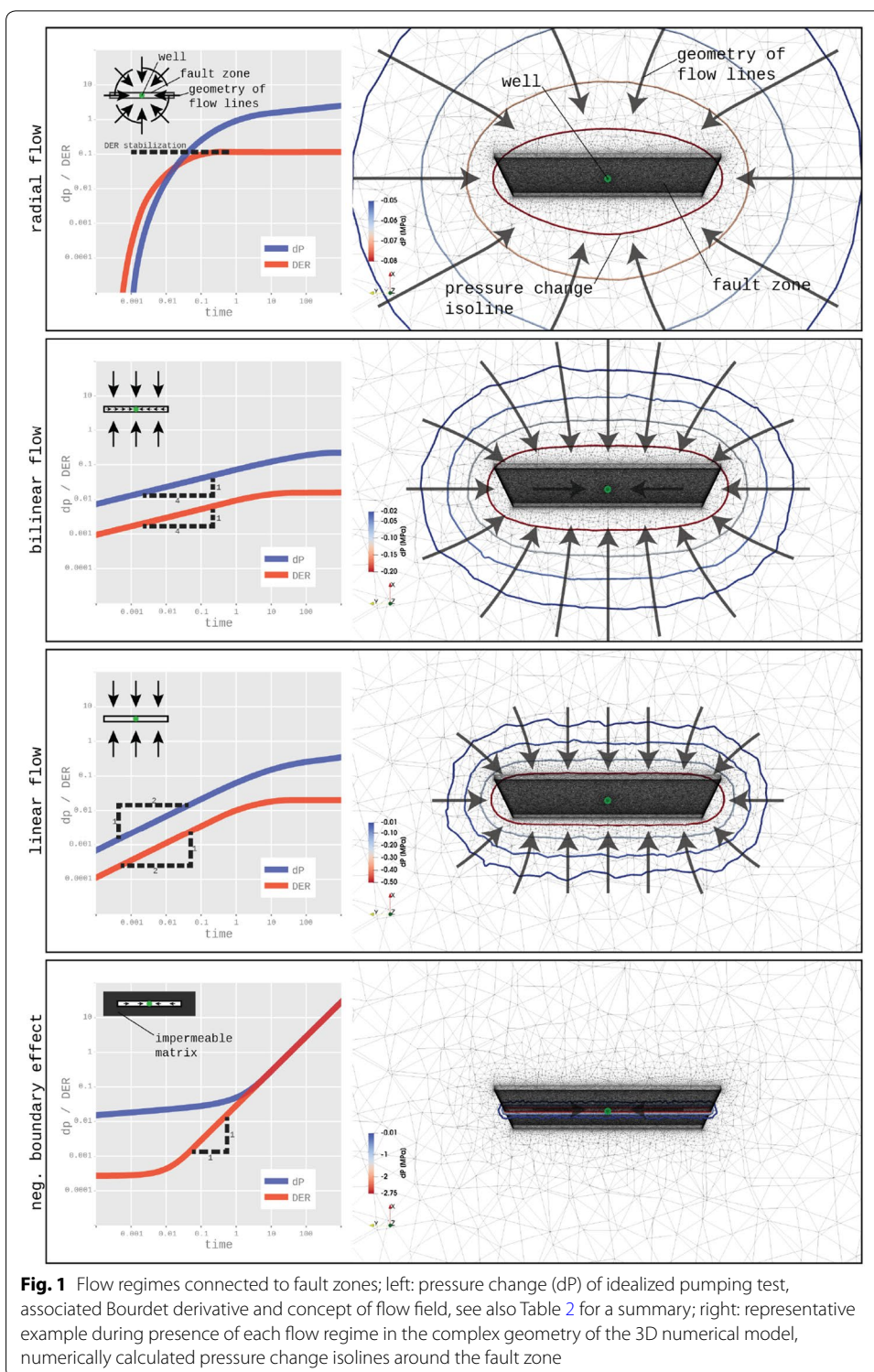
**Fig. 1** Flow regimes connected to fault zones; left: pressure change (dP) of idealized pumping test, associated Bourdet derivative and concept of flow field, see also Table 2 for a summary; right: representative example during presence of each flow regime in the complex geometry of the 3D numerical model, numerically calculated pressure change isolines around the fault zone

characteristic Bourdet derivative and a concept of the flow field. These flow types will be further explained in "Methods" section: "Pressure data evaluation." Additionally, representative results of the numerical model for each flow regime are shown as pressure change isolines (right side).

## Methods

The following chapter highlights the methodology through which the subsequent results and interpretations were achieved. Figure 2 illustrates an overview of the actual workflow. Next, a short description to the individual steps is given for complementary context followed by a more detailed explanation in the particular method sections.

At first, a suitable hydrogeological concept was chosen that incorporates all hydraulic elements and their geometry as well as ranges for all relevant properties. This information was then transformed into a tetrahedral mesh describing the investigated aquifer spatially. Combining this mesh with the physics of interest, a numerical model was set up for the simulation of pumping tests with different hydraulic property combinations. To prove the plausibility of this model, field data of a geothermal well with linear flow were used for calibration and associated validation. Next, an adaptation of the pressure transient analysis methodology was developed to automatically evaluate a large number of simulated pumping test data. By investigating the sensitivity of the hydraulic model properties, all those of relevance could be retrieved and further used for a systematic parameter study. In this study, the parameter space was sampled and the corresponding model response, the pumping test, calculated. These results were then scanned for parameter combinations that mark the transitions between the occurring flow regimes. With the help of a regression analysis based on these identified parameter combinations, a continuous visualization for the input parameter space could be achieved. A constitutive interpretation of the flow regime transitions was therefore possible.

### Hydrogeological concept

A conceptual model representing the main controlling hydraulic elements on a reservoir scale is first created as a basis for the numerical model representing the conditions in the targeted aquifer (Bundschuh and Suárez Arriaga 2010). For the investigation of pumping tests in the Malm aquifer, those main elements are the aquifer matrix and the fault zones.

The term aquifer matrix summarizes here all heterogeneities on a scale lower than the reservoir scale (e.g., small-scale facies changes or individual fractures) and describes it



**Fig. 2** Summary of workflow steps and their purpose
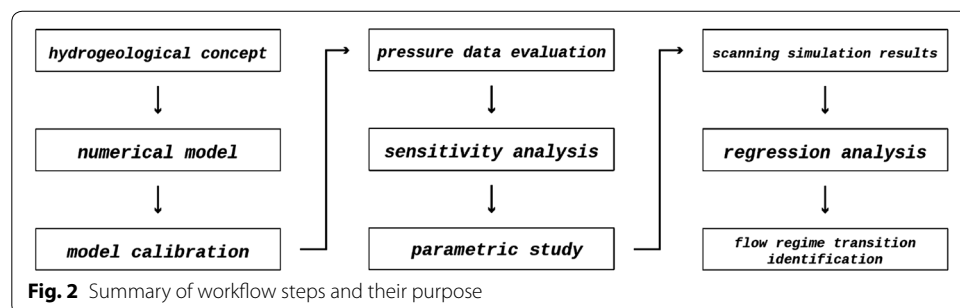
as a continuum with averaged properties forming a representative elementary volume (REV) after Bear (1972). Changes in rock types and properties on a scale relevant to the numerical simulation of the hydraulic reservoir behavior are controlled by the larger-scale lithofacies and diagenesis in the southern German Molasse Basin. Böhm et al. (2013) presented a hydrostratigraphic classification of the Malm aquifer based on these two main factors and the data of 17 wells. This classification followed the stratigraphic grouping of Quenstedt (1858). Here, the two units Lower to Middle Malm (Malm delta and epsilon) and Upper Malm (Malm zeta) are generally considered as the aquifer. The thickness and actual hydraulic properties are varying depending on the individual facies position. For the purpose of this investigation, an average value of 500 m (Böhm et al. 2013; Fritzer 2012; Stier and Prestel 1991) was considered as sufficient to represent the typical aquifer thickness. Note that the goal of this work is not to represent the spatial heterogeneity but considers the integrated hydraulic behavior at a well site. The hydraulic matrix properties (specific storage and permeability) were accordingly averaged on the chosen thickness, which also allows an application of the model results on different aquifer thicknesses.

As mentioned in the introduction and presented in more detail in Cacace et al. (2013), fault zones can be hydraulically grouped into three types: (1) transparent to fluid flow; (2) highly permeable conduit; (3) barrier due to impermeable fault core while surrounded by highly permeable damage zone. Since the focus of this work is to describe those fault zones that positively influence the productivity of a well, type 3 is not considered in the presented analysis. But types 1 and 2 as well as the transitions between them are subject of this work and are implemented also through a REV and the variation of its averaged hydraulic properties. In order to incorporate typical fault zones as such an REV in the hydrogeological concept, their geometries had to be characterized. The dip angle of the majority of faults in the Molasse Basin varies between 60° and 85°. This is based on available seismic data from five different locations (Weilheim, Dürrnhaar, Kirchstockach, Sauerlach, Geretsried) and also on the work of Moeck et al. (2015), von Hartmann et al. (2016) and Lüschen et al. (2014). Throw values of these ENE-WSW-trending normal faults are known to range from 25 to 300 m (Bachmann et al. 1987, 1982; Moeck et al. 2015; Schneider and Thomas 2012). On the other hand, few data are available to quantify their lateral extent. But as correlations between throw and thickness or observations in similar rock layers suggest, values between 10 and more than 100 m are possible (Agosta and Aydin 2006; Michie et al. 2014). It is not necessary to incorporate the actual fault throw into the hydrogeological concept since these fault zones generally extend beyond the aquifer host rock. Hence, only the fault zone thickness remains as important geometric value and was therefore integrated into the numerical investigations based on the mentioned range. The fault zone length has been fixed to a value of 1000 m and the fault inclination to a value of 70°. Both were derived from the previously mentioned seismic information and chosen as mean characteristic values.

Besides information about the geometry of the introduced main hydraulic elements, it is necessary to know the relevant properties of their corresponding host rock. Available data were therefore gathered from literature and field engineers (ERDWERK GmbH) and are summarized in Table 1 for all parameters relevant to a hydraulic simulation. Information about the fluid viscosity is based on pure water properties of the NIST

**Table 1 Possible ranges for the hydraulic parameters of the Malm aquifer; unit conversions calculated for a fluid density of 971.82 kg/m$^3$ and a fluid viscosity of 2.89 × 10$^{-4}$ Pa s (30 MPa pore pressure and 100 °C reservoir temperature)**
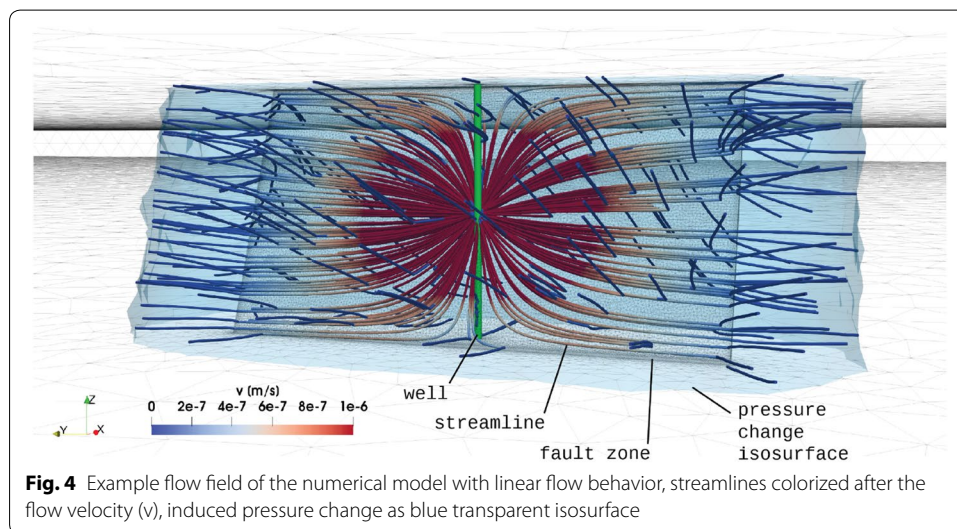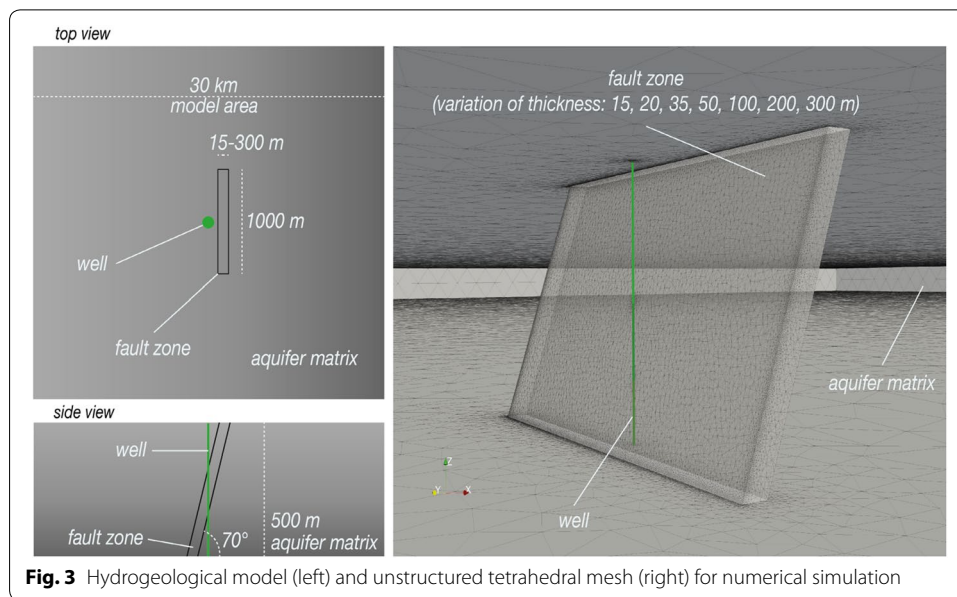
| $x_i$ | $i$ | Min | Max | Unit | Sources |
|---|---|---|---|---|---|
| Matrix permeability | 1 | $1.0 \times 10^{-17}$ | $1.0 \times 10^{-12}$ | m$^2$ | Birner (2013) |
|  |  | $3.3 \times 10^{-10}$ | $3.3 \times 10^{-5}$ | m/s | TUM (2019) |
| Matrix storage | 2 | $2.0 \times 10^{-12}$ | $1.6 \times 10^{-10}$ | 1/Pa | TUM (2019) |
|  |  | $2.0 \times 10^{-8}$ | $1.6 \times 10^{-6}$ | 1/m |  |
| Fault zone permeability | 3 | $1.0 \times 10^{-14}$ | $1.0 \times 10^{-9}$ | m$^2$ | Birner (2013) |
|  |  | $3.3 \times 10^{-7}$ | $3.3 \times 10^{-2}$ | m/s | TUM (2019) |
| Fault zone storage | 4 | $2.0 \times 10^{-12}$ | $1.6 \times 10^{-10}$ | 1/Pa | TUM (2019) |
|  |  | $2.0 \times 10^{-8}$ | $1.6 \times 10^{-6}$ | 1/m |  |
| Fault zone thickness | 5 | 15 | 300 | m | Agosta and Aydin (2006); Michie et al. (2014) |
| Fluid viscosity | 6 | $1.0 \times 10^{-4}$ | $3.0 \times 10^{-4}$ | Pa s | NIST (Lemmon et al. 2018) |
| Production rate | 7 | 20 | 90 | l/s | Geotis (Agemar et al. 2014) |

Chemistry WebBook, while production rates were taken from the Geothermal Information System (Agemar et al. 2014; Lemmon et al. 2018). A permeability range for the Malm aquifer is available in Birner (2013). A range for the permeability and specific storage values of the Malm aquifer was gathered from unpublished reports in collaboration with the research project Geothermal Alliance Bavaria and is based on the evaluation of 17 interference tests in the area of Munich (TUM 2019). The advantage of using the results from these tests is that they describe the average reservoir behavior between two exploration wells and therefore represent the properties of the chosen REV. Small-scale heterogeneities are not of interest which would influence laboratory data. An extension by approximately an order of magnitude of these collected ranges assures a conservative approach (see Table 1).

### Numerical model

As it is the aim to exactly reproduce the geometric complexity of the previously presented concept while mathematically describing its hydraulic state, a numerical approach was chosen over an analytical one due to its geometric freedom. For this the numerical simulator MOOSE framework (Gaston et al. 2009) combined with the reservoir simulation app GOLEM (Cacace and Jacquey 2017a), the mesh-generation-program MeshIT (Blöcher et al. 2015) and the visualization-plus-pre-/post-processing-tool Paraview (Ahrens et al. 2005) were chosen. The combination of these open source tools allows for a continuum approach together with discrete elements in an unstructured tetrahedral mesh, state-of-the-art numerical solvers and preconditioners, as well as parallelization capacities, suitable for high-performance supercomputers. This guarantees a precise consideration of the geometry and a fast and efficient approach to calculate the pressure evolution during a pumping test for different parameter combinations.

The model setup can be summarized in the following way (Fig. 3). The aquifer is represented with homogeneous properties, a thickness of 500 m and a lateral extent of 30 × 30 km (no flow boundaries). A 70°-inclined and 1000-m-long fault zone is located in the middle of this permeable rock layer, with a vertical well in its center (see

**Fig. 3** Hydrogeological model (left) and unstructured tetrahedral mesh (right) for numerical simulation



**Fig. 4** Example flow field of the numerical model with linear flow behavior, streamlines colorized after the flow velocity (v), induced pressure change as blue transparent isosurface

"Hydrogeological concept" section). The fault zone thickness should be variable and is integrated as independent variable into the parameter study.

The described geometries were represented in a tetrahedral mesh (Fig. 3) consisting of two continua: first, the host rock (further called matrix); second, the fault zone; and additionally a discrete lower-dimensional element, that depicts the borehole, at which the production sink was applied. For each fault zone thickness of the parameter variation, a separate mesh was generated. As the observation of the hydraulic response of a faulted reservoir to water extraction is the goal, a calculation of fluid flow by Darcy's law is sufficient. Equation (1) presents the relevant mass balance equation as it is integrated in the GOLEM simulator (Cacace and Jacquey 2017b). Since GOLEM is capable of coupling thermal, hydraulic and mechanical behaviors of a porous medium, (1) gets

simplified for pure hydraulic calculations into Eq. (2) with the Darcy velocity as in (3). Figure 4 shows an example simulation result. The applied water extraction in the well induces a pressure change which is shown as a transparent isosurface, while the corresponding streamlines are colorized according to the local flow velocity.

$$\text{Mass Balance Equation} \quad \frac{\partial (n\rho_f)}{\partial t} + \nabla \cdot (n\rho_f \boldsymbol{v}_f) - Q_f = 0 \tag{1}$$

$$\text{Pore Pressure Equation} \quad \frac{n}{K_f} \frac{\partial p_f}{\partial t} + \nabla \cdot \boldsymbol{q}_D - Q_f = 0 \tag{2}$$

$$\text{Darcy's Law} \quad \boldsymbol{q}_D = -\frac{\boldsymbol{k}}{\mu_f} (\nabla p_f - \rho_f \boldsymbol{g}) \tag{3}$$

$n$ = porosity,      $\boldsymbol{q}_D$ = Darcy's velocity,      $p_f$ = pore pressure,      $Q_f$ = sink/source, $\rho_f$ = fluid density,      $\boldsymbol{k}$ = permeability tensor,      $t$ = time,      $\boldsymbol{g}$ = gravity vector, $\mu_f$ = fluid viscosity, $K_f$ = fluid bulk modulus, $\boldsymbol{v}_f$ = fluid velocity.

### Calibration with field data

Before the desired investigation on the behavior of fault zones in the Malm aquifer's pumping tests can be carried out with confidence, it is necessary to calibrate the numerical model (Bundschuh and Suárez Arriaga 2010). Hydraulic data of a geothermal exploration site in the area of Munich that exhibits a flow regime dominated by a fault zone were available for the verification of the chosen model concept. These data comprise the pressure evolution of a 96-h-long pumping test, which includes a 24-h-long recovery phase, and the associated production rates. By choosing a starting point inside realistic parameter ranges (see Table 1 and "Sensitivity analysis" section) and varying fault zone thickness, specific fault zone storage and permeability as well as specific matrix storage and permeability until the pressure change and DER of the recovery phase could be matched and a first calibration was carried out (see also "Pressure data evaluation" section for the underlying methodology). Next, the calibration was tested against the actual production history. These two steps were repeated until recovery and production history could both be appropriately matched (see "Results" section for the actual calibration)

### Pressure data evaluation

The core method for well test interpretation of transient pressure data (pressure transient analysis, PTA) is the pressure derivative (DER), also called Bourdet derivative (Bourdet 2002; Bourdet et al. 1983). It is defined as in (4).

$$\text{Bourdet derivative (DER)} \quad \Delta p' = \frac{dp}{d \ln \Delta t} = \text{DER} \tag{4}$$

$p$ = pore pressure, $t$ = time.

By plotting the DER together with the corresponding pressure change in the same log–log graph, characteristic shapes, defined by their slopes, for various flow regimes can be observed and quantified through analytical models. This method is in practice mostly only applied on the recovery phase of a pumping test due to no fluctuations in

Konrad *et al. Geotherm Energy*      (2019) 7:25

Page 10 of 28

the production rate. A selection of the most common flow regimes is given in Gringarten (2008). Bourdet (2002) summarized the definitions and use of corresponding interpretation models in a comprehensive overview. For the investigation of a fault zone's influence in a real-world parameter space on the hydraulic response of a geothermal well, the middle to late timescale of the pressure data and the following interpretation models are of main interest: radial flow, bilinear flow, linear flow and negative boundary effect (also called closed homogenous reservoir) (see also Fig. 1). Naturally, it comes to mind that those defined models have smooth transitions from one to another inside the combinations of natural parameter ranges. A radial flow regime is expected to occur if the influence of the fault zone is just minor and the pressure front propagates into the reservoir homogeneously. If the hydraulic properties of the fault zone improve relative to the surrounding matrix, an increase in the slope of the derivative is expected. At some point, the pressure change and corresponding derivative will reach a slope of 0.25 at the same time. This is when a bilinear flow regime is fully present. Here, the pressure drop inside the fault zone is still significant and two linear flow geometries are present (in the matrix perpendicular to the fault zone and inside the fault zone parallel to its surfaces) (Bourdet 2002). A same shift in the DER slope should also happen from bilinear flow to linear flow (increase in the pressure change and derivative slope from 0.25 to 0.5) if the fault zone properties improve more. This is when the pressure drop inside the fault zone becomes instant and only a linear flow geometry inside the reservoir perpendicular to the fault zone is present (Bourdet 2002). With an even higher hydraulic significance of the fault zone, the slopes will increase until they reach a value of 1.0, in which case the matrix around the fault zone is basically not producing any water to the well and exhibits a negative boundary effect. Here, there reservoir starts to deplete as soon as the pressure front reaches the end of the fault zone (Bourdet 2002).

Therefore, a definition is necessary to classify which flow observations are assigned to one of the previously named flow regimes in a continuous parameter space. Table 2 shows the characteristic properties of the previously mentioned flow regimes relevant to this work and also the definition that was chosen to automatically classify transient pressure observations in the parameter space of the Malm aquifer. The selected classes are based on the analytical interpretation models and should reflect how a field engineer would classify the pressure curves in practice.

**Table 2 Characteristic properties of the flow regimes of interest; analytical model versus classification for real-world parameter space**

| Flow type | Radial | Bilinear | Linear | Negative boundary |
|---|---|---|---|---|
| Analytical model properties | | | | |
|   dP slope | – | 0.25 | 0.5 | 1 |
|   DER slope | 0 | 0.25 | 0.5 | 1 |
|   Additional properties | – | At the same time | At the same time | DER slope over a log cycle early at slope 1 than dP |
| Classification for automated PTA | | | | |
|   dP slope | – | 0.15–0.375 | 0.375–0.6 | 0.6–1.0 |
|   DER slope | 0–0.15 | 0.15–0.375 | 0.375–0.6 | 0.6–1.0 |

**Exploration of parameter space**

The first step for an efficient exploration of the parameter space is its definition. Therefore, a sensitivity analysis was carried out to find all parameters that are of importance. This is described more in detail in "Sensitivity analysis" section of the results.
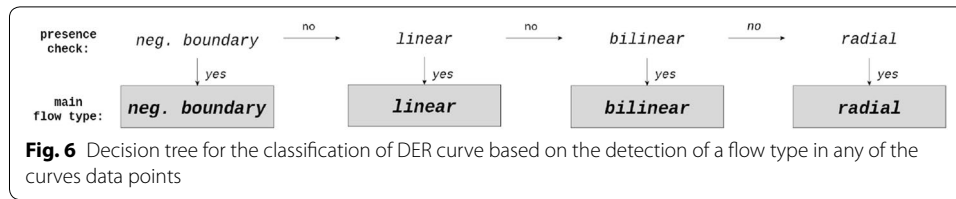
For the description of transitions between the different flow regimes in the defined parameter space, pumping tests for as many parameter combinations as possible have to be simulated. The time span over which pumping tests gather hydraulic data in practice is generally only a few days long. Additionally, in the field only the recovery phase data of these tests are suitable for a proper evaluation of the well and reservoir properties since they are technically not possible to produce water under a constant rate during drawdown (Alt and Kahnt 2014; Bourdet 2002). So the actual field data for evaluation by a reservoir engineer have an even shorter time span. For the simulated pumping tests, a time of 500 h was set as extreme value that would always be longer than any pumping test carried out in reality for the Malm aquifer. In addition, the difficulty of keeping a constant production rate does not apply for the numerical model. This allows for directly calculating only the pressure drawdown, which reduces the simulation time.

With the application of RAVEN, an open source software framework for parametric and stochastic analysis (Alfonsi et al. 2017), and the use of an HPC cluster [LRZ Linux cluster and Supermuc (Leibniz-Rechenzentrum 2017)], it is possible to calculate a great number of artificial pumping tests in a reasonable time. To use those computational resources efficiently, an adequate temporal and spatial discretization of the individual numerical simulations is necessary without introducing numerical errors or unnecessary inaccuracies for further evaluation. First, this can be ensured by choosing an adaptive time stepping scheme based on the difficulty of the solution with an initial time step size of one second and an appropriate growth factor (the previous time steps get multiplied by this factor if the number of iterations is below a threshold) (Idaho National Laboratory 2019). For the determination of a suitable value for this factor, an optimization was carried out. An example parameter combination that exhibits linear flow was chosen to compare different growth factors to the resulting total number of time steps and the accuracy of the DER calculation. As can be seen from Fig. 5, growth factors above 2.0 decrease the length and accuracy of the DER curve significantly. At the same time, an exponential increase in the total number of time steps can be observed for the values 1.1 and 1.2. Therefore, a growth factor of 1.6 with a resulting total time step number of 30 was set for the discretization of the proposed 500 h simulation time. Regarding the spatial discretization, a second optimization was conducted. For every fault zone thickness investigated in the parametric analysis, a separate mesh was generated (see also "Numerical model" section). In a first step, the main goal was to construct a visual appropriate representation of the desired geometry while keeping the total number of tetrahedral elements low to enable a fast simulation. This resulted in mesh element numbers ranging from ~0.45 million (300-m fault zone thickness) to ~1.3 million (15-m fault zone thickness) elements. To investigate whether this discretization was sufficient, a test case was calculated for each mesh and then compared against the same case but with a global mesh refinement of one level (each existing tetrahedral was split into four child elements). The results showed that the calculated pressure values varied between the refined and the normal mesh version by an average of about 0.02%. This variation

**Fig. 5** Influence of temporal discretization on simulation result; initial time step = 1 s
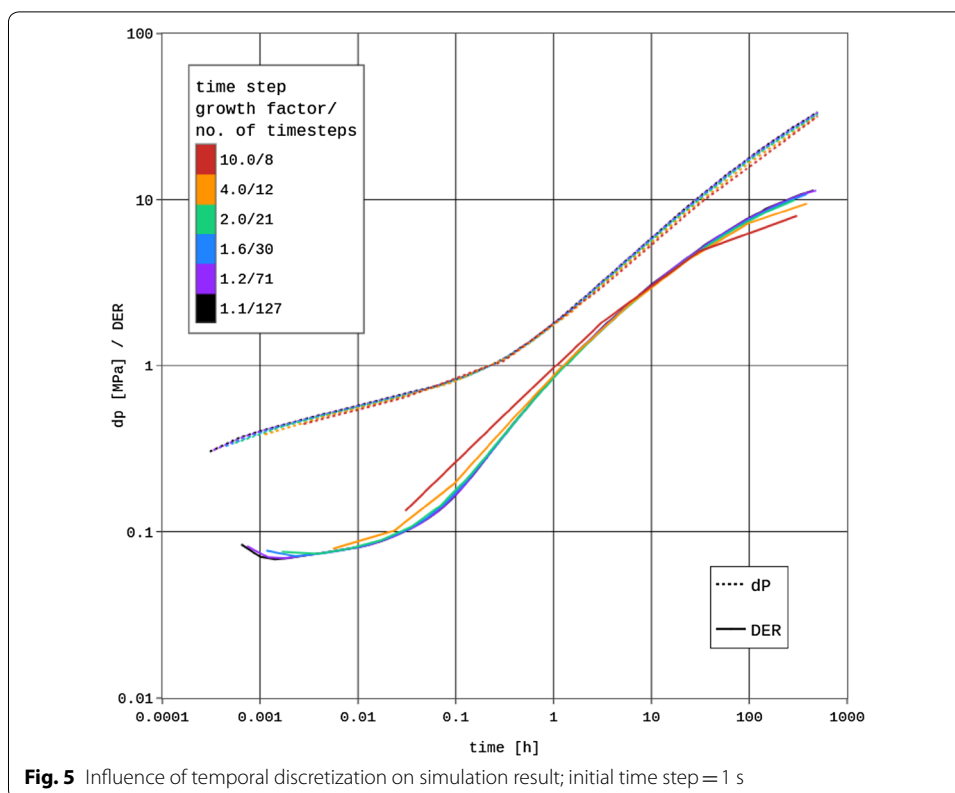
influenced the Bourdet derivative evaluation only in the first two to four time steps, while in the remaining ones no visual difference could be noticed. Because the early time behavior of the derivative isn't of interest to the main analysis (see "Pressure data evaluation" section), we accepted the unrefined meshes for the main parametric analysis. On a normal workstation (Intel® Core™ i7-4790K CPU @ 4.00 GHz), the resulting simulation times ranged from ~37 min (15-m fault zone thickness) to ~9 min (300-m fault zone thickness). By running the numerical model on an HPC system (lrz linux cluster; Intel® Xeon® E5-2697 v3), these times reduced to ~24 min (15-m fault zone thickness) and ~4 min (300-m fault zone thickness). Additionally, many simulations can be calculated simultaneously which reduces the overall time needed drastically.

After the basic numerical model was set up, a sampling scheme had to be chosen to scan the input space with the goal to explore the system response in terms of the pressure evolution over time. For that, the grid sampling method was chosen, which discretizes the parameter ranges in a user-defined number of intervals and combines them into a grid. The model was then simulated at each coordinate and the response captured for further evaluation (Alfonsi et al. 2017). The grid was set, limited by the simulation time and the available computational resources and based on the possible parameter ranges listed in Table 1, to 11 values, logarithmically evenly spaced, for fault zone and matrix permeability, six values, linearly evenly spaced, for specific fault zone and matrix storage and seven values for the fault zone thickness (15, 20, 35, 50, 100, 200 and 300 m). The resulting parameter grid is made up of 30,492 input-space-coordinates/parameter combinations.

**Fig. 6** Decision tree for the classification of DER curve based on the detection of a flow type in any of the curves data points

The next step after carrying out the parametric study is the investigation of the produced simulation results (see Fig. 2). To determine the corresponding flow regime of each result, an automation of the necessary pressure transient analysis (PTA) was implemented in Python. In detail, for each sampled parameter combination, the DER was calculated and each data point in time was classified based on the previously presented characteristics (Table 2). Afterward, this classification in time was reduced to the main occurring flow regime following a decision tree (Fig. 6). As a next step, sampled points at the boundary between the occurring flow regimes were extracted from the 30,492 input-space-coordinates and as individual data sets for each flow regime boundary (radial to bilinear, bilinear to linear, linear to neg.-boundary) separated. These data sets represent the transition between the fault zone-related flow regimes as point data. To get a functional relationship for a continuous visualization of the boundary data sets in the investigated parameter space, a polynomial regression was applied. Therefore, one target variable ($y$, see Appendix 1) among all the investigated hydraulically sensitive parameters ($x_i$, see Appendix 1) had to be chosen, while the remaining ones were used as explanatory/predicting variables. Since the matrix permeability has the highest relevance for the field application, as it is one of the main results of pumping tests, it was set as $y$. Depending on these two variable types, each boundary data set was split into a predictor data set ($X$) and a target data set ($Y$) on which the regression model was fit. Since a polynomial regression is a special case of a linear regression, the same principle of minimization of residual sum of squares between observed data set responses and by the regression model predicted responses through fitting coefficients applies (Draper and Smith 1998). The Python package "scikit-learn" was utilized to achieve this (Pedregosa et al. 2011). Scaling of the underlying data set (extracted flow regime boundary data points) according to Eq. (5) was introduced to increase numerical stability of the regression (Buitinck et al. 2013; scikit-learn user guide: preprocessing data 2018). The respective scaling information which forms the base for all further steps of the regression analysis is provided in Appendix 2. The determination of a suitable polynomial degree was done by calculation of the adjusted coefficient of determination for the degrees from 1 to 12.

$$\text{Data set scaling} \quad X_{i,j,\text{scaled}} = \frac{X_{ij} - \overline{X_i}}{\sigma_i} \tag{5}$$

$X_{i,j,\text{scaled}} = j$-th scaled value of $i$-th predictor ($x_i$) training data set,
$X_{ij} = j$-th value of $i$-th predictor ($x_i$) training data set,
$\sigma_i$ = standard deviation of training data set for $i$-th predictor,
$\overline{X_i}$ = mean of training data set for $i$-th predictor.

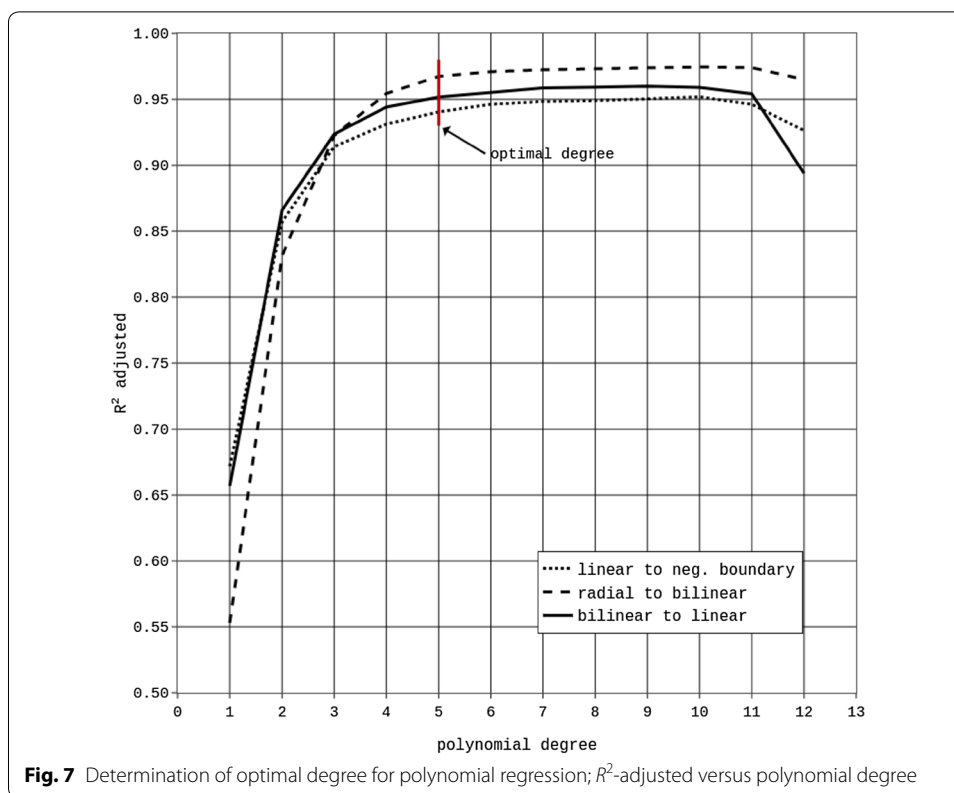**Fig. 7** Determination of optimal degree for polynomial regression; $R^2$-adjusted versus polynomial degree

Figure 7 shows the adjusted coefficient of determination ($R^2_{\text{adjusted}}$) versus the polynomial degree for the regression of the three transitions of interest (between the radial, bilinear, linear and negative boundary flow regime). The change in $R^2_{\text{adjusted}}$ from degree five to degree six of the polynomial drops below 1% for all three transitions. Hence, degree five was used for the regression analysis. Subsequent visualization and interpretation of the presence of a flow regime in the investigated parameter space were built upon the resulting polynomial relationship. The corresponding regression functions are provided in Appendix 3.

## Results

The following section presents the results of the work flow to identify the transitions between occurring flow regimes associated with fault zones for the Malm aquifer (radial, bilinear, linear and negative boundary flow).

### Calibration

As previously explained, a calibration and validation against a pumping test of a geothermal well in the south of Munich that exhibits linear flow was done before the desired parametric study could be tackled with confidence. After approximately 500 simulation runs, a best fit between modeled and measured pumping test data could be achieved. Figure 8 shows a comparison between the two. The "log–log plot of recovery phase" illustrates the calibration fit on the recovery pressure data. The validation is shown in "complete pumping test history" where the calibration was tested against the varying
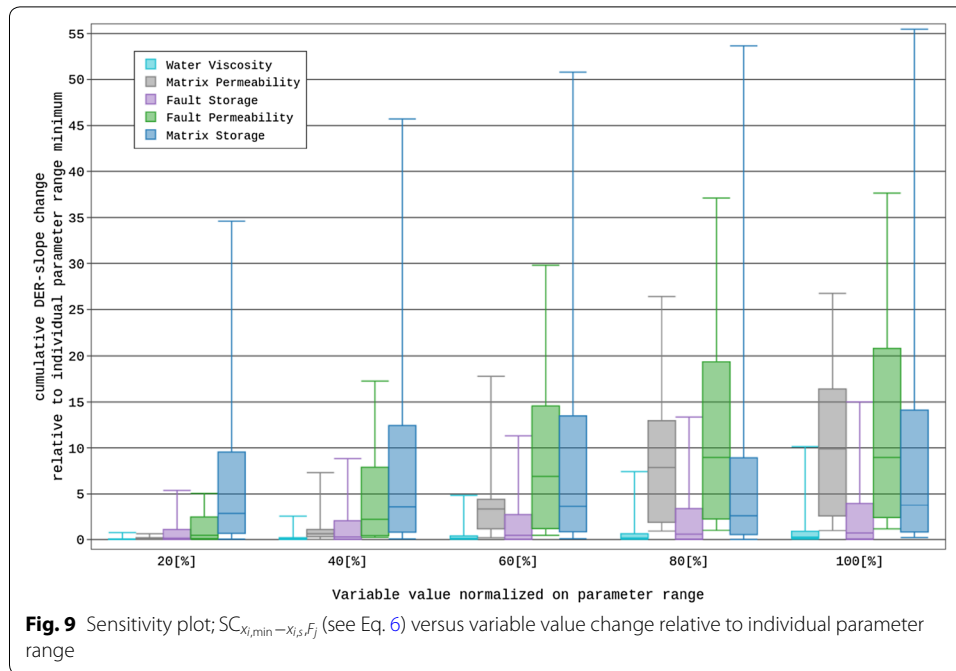
**Fig. 8** Calibration results; left: log–log plot of recovery phase; right: pressure and rate history of complete pumping test
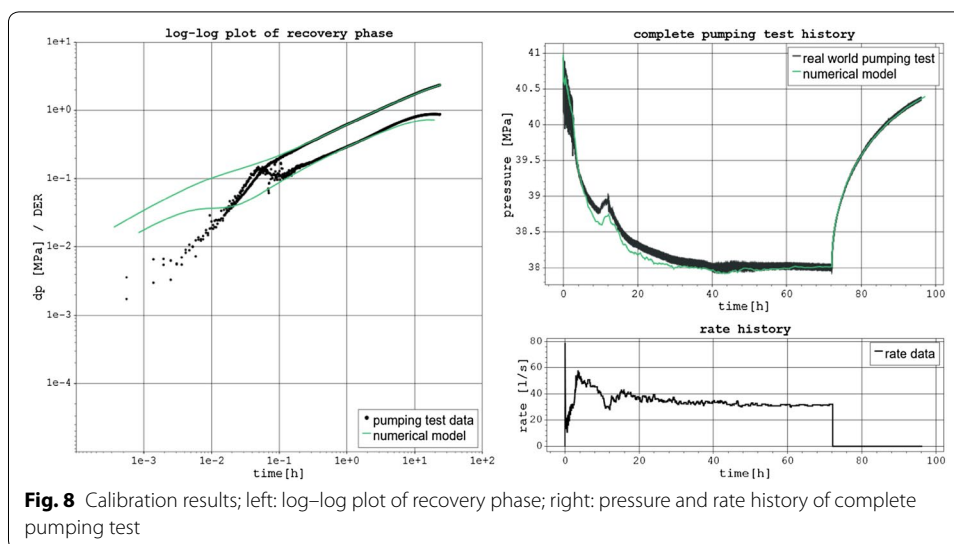
production rates of the test. The final calibration/validation values are: 15 m fault zone thickness, $8.8 \times 10^{-16}$ m$^2$ matrix permeability, $2.2 \times 10^{-12}$ 1/Pa specific matrix storage, $1.0 \times 10^{-9}$ m$^2$ fault zone permeability, $2.0 \times 10^{-12}$ 1/Pa specific fault zone storage and positive boundary with a distance of approximately 400 m to the well.

### Sensitivity analysis

As previously stated, a determination of all sensitive parameters is necessary. In the context of pressure transient analysis, individual parameter influence can be measured by the shape change of the DER curve depending on that parameter's variation. The following parameters were subject to this sensitivity analysis: specific storage of fault zone and matrix, permeability of fault zone and matrix, production rate, fault zone thickness, fluid viscosity. The spectrum of these properties has been gathered for the Malm aquifer in Table 1 (see "Hydrogeological concept" section).

Each of the hydraulic properties listed above ($x_i, i = 1, 2, \ldots, 7$) was sampled by six values ($x_{i,s}, s = 1, 2, \ldots, 6$) evenly spaced (log spaced for fault zone and matrix permeability) over its possible range for each combination among maxima and minima of the remaining parameters (further called fixations $F_j, j = 1, 2, \ldots, 2^{i_{\max}-1=6}$) and their corresponding ranges. Six parameter perturbations in this one-at-a-time approach were chosen compared to the recommended minimal number of three (endpoints and midpoint of parameter range) to increase the accuracy of the sensitivity analysis (Petropoulos and Srivastava 2017). That resulted in the calculation of $6 * 2^6 = 384$ simulations and their DER curves for all parameters of interest with the exception of the fault zone thickness since it is necessary to generate a new mesh every time this parameter needs to be varied. Additionally, fault zone thickness values below 100 m are more realistic as stated before (see "Hydrogeological concept" section). This eventually resulted in a manual perturbation for this parameter of five unevenly spaced values (20, 35, 50, 100 and 200 m) with the focus on lower fault zone thicknesses ($5 * 2^6 = 320$). The DER shape changes between the six, respectively five, values of the investigated parameters were compared relative to the DER curve at parameter range minimum, $\text{DER}_{x_{i,\min}, F_j}$. The quantification of the DER shape change between the two

Konrad *et al. Geotherm Energy* (2019) 7:25

Page 16 of 28



**Fig. 9** Sensitivity plot; $SC_{x_{i,\min}-x_{i,s},F_j}$ (see Eq. 6) versus variable value change relative to individual parameter range

**Table 3 Median values of $SC_{x_{i,\min}-x_{i,s},F_j}$ for the evenly/log-evenly spaced parameters**

| Variable value normalized on parameter range [%] | Water viscosity | Matrix permeability | Fault zone storage | Fault zone permeability | Matrix storage |
|---|---|---|---|---|---|
| 20 | 0.017 | 0.058 | 0.149 | 0.441 | 2.819 |
| 40 | 0.058 | 0.620 | 0.270 | 2.189 | 3.522 |
| 60 | 0.113 | 3.297 | 0.444 | 6.914 | 3.590 |
| 80 | 0.177 | 7.870 | 0.570 | 8.968 | 2.578 |
| 100 | 0.245 | 9.893 | 0.691 | 8.972 | 3.759 |

compared curves ($SC_{x_{i,\min}-x_{i,s},F_j}$) was done according to Eq. (6), by summarizing the quadratic differences of the first derivative of the DER in each data point in time. This resulted in five (four, for fault zone thickness) DER shape change values per investigated parameter for each of the $2^6 = 64$ fixations ($F_j$). Through normalizing each parameter variation on its parameter range, a comparison of the sensitivity between all hydraulic properties is possible (Petropoulos and Srivastava 2017).

$$\text{DER shape change} \quad SC_{x_{i,\min}-x_{i,s},F_j} = \sum_{k=1}^{\max} \left( DER'_{x_{i,\min},t_k} - DER'_{x_i,t_k} \right)^2 \tag{6}$$

$SC$ = shape change measure,
$x_{i,s} = s$-th sampled$(s = 1, 2, \ldots, 6)$value of the investigated parameter $x_i$ ($i = 1, 2, \ldots, 7$,
$x_{i,\min}$ = minimum value of the investigated parameter range,
$F_j = j$-th fixation of the currently not investigated parameters, $\quad j = 1, 2, \ldots, 2^{i_{\max}-1=6}$,
$t_k = k$-th data point in time, $DER'$ = first derivative of the Bourdet Derivative

**Table 4  Median values of SC$_{x_{i,\min}-x_{i,s},F_j}$ for the unevenly spaced fault zone thickness**

| Variable value normalized on parameter range [%] | Fault zone thickness |
| --- | --- |
| 8 | 0.114 |
| 17 | 0.251 |
| 44 | 0.476 |
| 100 | 0.804 |

Figure 9 illustrates the calculated changes in the DER shape depending on specific storage, permeability and fluid viscosity. Specific matrix storage (max. median of SC$_{x_{2,\min}-x_{2,s},F_j} = 3.7$), fault zone (max. median of SC$_{x_{3,\min}-x_{3,s},F_j} = 8.9$) and matrix (max. median of SC$_{x_{1,\min}-x_{1,s},F_j} = 9.8$) permeability show the biggest influence on the shape of the DER. Specific fault zone storage (max. median of SC$_{x_{4,\min}-x_{4,s},F_j} = 0.6$) on the other hand shows only low sensitivity, while fluid viscosity (max. median of SC$_{x_{6,\min}-x_{6,s},F_j} = 0.2$) appears to have the lowest. From Tables 3 and 4, it is noticeable that the production rate has no influence, which was already to be expected as Bourdet et al. (1989) state that the speed of the pressure front propagating into the reservoir is independent of the flow rate. Fault zone thickness (max. median of SC$_{x_{5,\min}-x_{5,s},F_j} = 0.8$) and specific fault zone storage have an influence in the same low order of magnitude. Fluid viscosity can have an influence on the derivative shape but only to such a small extent that it was excluded from the further flow regime analysis. The resulting parameters, considered as sensitive, are the permeability and specific storage of fault zone and matrix as well as the fault zone thickness. The remaining insensitive parameters have been fixed for the flow regime analysis (production rate: $30\frac{l}{s}$, fluid viscosity: 0.0002897 Pa s).

### Identification of flow regime transitions in parameter space

As discussed previously, through grid sampling the parameter space (Table 1), calculation of the numerical model response, automated flow regime classification of the model output, extraction of parameter combinations at the flow regime transitions and a subsequent regression analysis, an appropriate visualization of these interfaces was possible (see "Methods": "Exploration of parameter space" sections).

The results of this regression are shown in Fig. 10 for selected characteristic settings. To show the fault zone thickness influence, two representative values (left column: 50 m, right column: 150 m) were visualized. Three graphs were generated for each fault thickness while every individual graph has a fixed specific matrix storage. The visualized axes were chosen with respect to the highest practical relevance which is on permeability values. The shift of the flow regime transitions due to specific fault zone storage is shown by four different line colors, and the line style depends on the flow regime transition type. Each drawn line represents the regression of parameter combinations at the transition between flow regimes according to the legend. Below that line (lower matrix permeability values), the occurrence of another flow regime is possible. Linear flow for example can be found below the solid and above or on the dotted line.

Konrad *et al. Geotherm Energy*     (2019) 7:25

Page 18 of 28
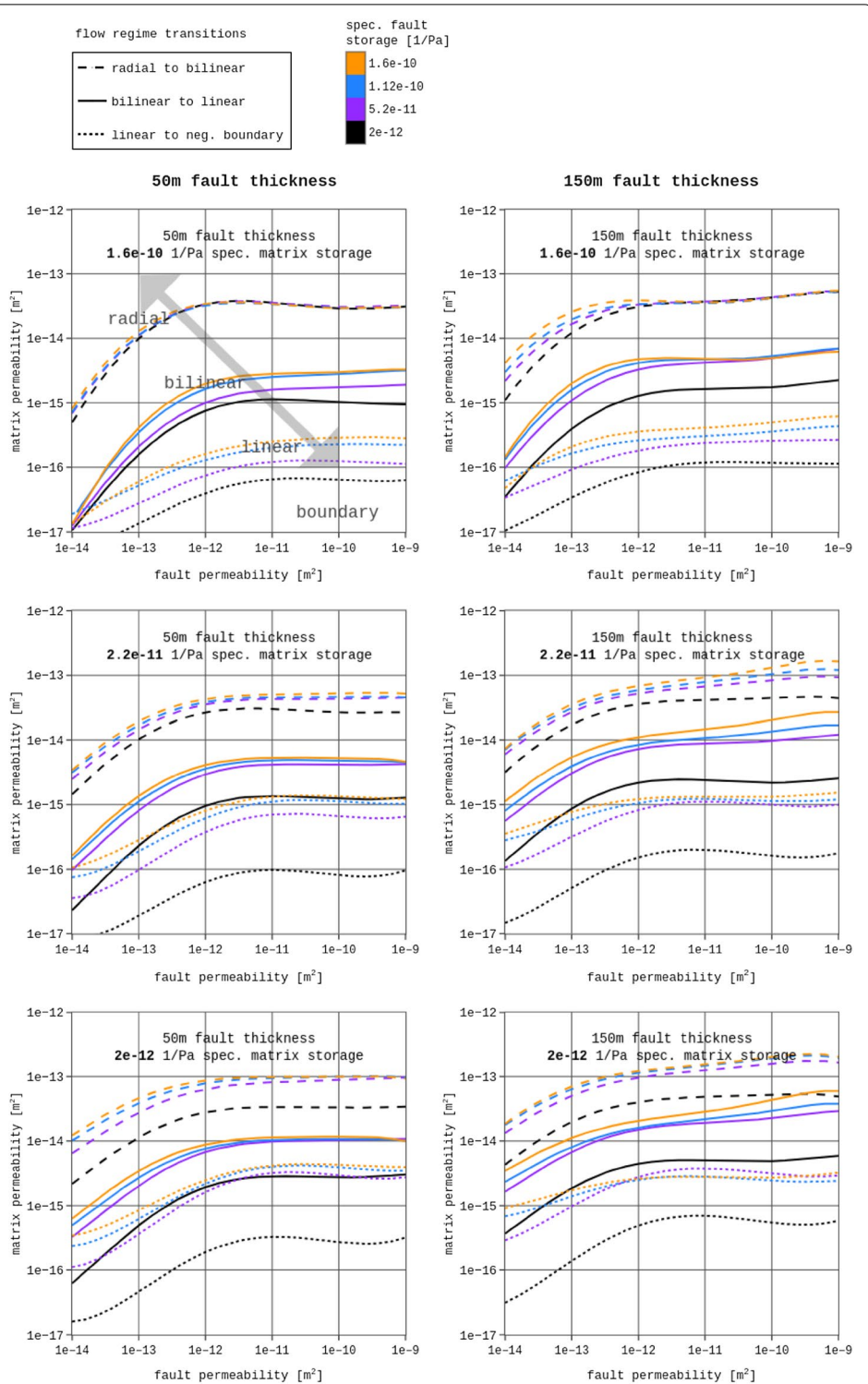


**Fig. 10** Regression results for characteristic parameter combinations for the three observed flow regime transitions (1: radial to bilinear, 2: bilinear to linear, 3: linear to negative boundary); left: 50 m fault zone thickness; right: 150 m fault zone thickness; subplots have fixed specific matrix storage values; specific fault zone storage color-coded; line styles represent the flow regime transitions; parameter combinations that fall on the transition line should be seen as combinations for which the flow regime above has still been observed

It can be observed that there is a nearly constant logarithmic slope at each flow regime transition for small permeability values of fault zone and matrix present. This slope starts to decrease at some point, while permeability values increase, which means that the influence of the increasing fault zones permeability declines until it is no longer present. So only the matrix permeability controls which flow regime is present when keeping a constant specific storage and a fixed fault zone thickness. The slope value itself is controlled by fault zone thickness and also specific storage of fault and matrix. In some cases of the transition between linear flow and negative boundary flow, it can be seen that the slope is not constant for extreme low-permeability combinations. It is also noticeable that for higher fault zone thickness and specific matrix storage values below 1.6e−10 1/Pa the slope does not reach zero for all flow regime transitions anymore.

Focusing on specific storage, it is visible that the values of the matrix and the fault zone are contradicting in its effects. Higher specific matrix storage lowers the permeability values at the flow regime transitions, while higher specific fault zone storage raises them. But looking at the size of the parameter window of linear flow, meaning the area in parameter space, it can be noted that increasing specific storage values of either fault zone or matrix are reducing its area. At the same time, the area of negative boundary style flow expands.

Table 5 summarizes matrix permeability values at the flow regime transitions for extreme settings. The flow regime noted in the column to its right is possible if matrix permeability values are smaller than this extreme value and equal to or bigger than the extreme value in the next column. The table has been derived from the corresponding regression functions for minimum and maximum values of specific fault and matrix storage and for the extreme fault permeability of 1.0e−9 m$^2$. To observe bilinear flow, which represents the weakest in pumping tests visible influence of a fault zone, for example with specific storage for matrix and fault of 2.0e−12 1/Pa and a fault zone thickness of 15 m, the matrix permeability has to be below 4e−14 m$^2$ and equal or above 3e−15 m$^2$.

By looking closer at the radial-to-bilinear transition, it can be seen that there is an area above that line which consists of parameter combinations with higher fault zone than matrix permeability. This means a pumping test observes only radial flow at those combinations even though the fault zone holds better hydraulic properties compared to the surrounding matrix. The size of this area in parameter space containing for pumping tests invisible but hydraulically enhancing fault zones is decreasing with a decline in the specific matrix storage. Extreme cases from Table 5 suggest that the observation of bilinear flow for the Malm aquifer is possible for the first time if matrix permeability values are below 2e−13 m$^2$ and if they drop below 6e−14 m$^2$ linear flow becomes feasible.

## Discussion

For the evaluation of the calibration results, it is important to note that the model focus is on fault zone and aquifer, while technical well conditions were simplified. Therefore, it can be seen that in the early time region of the recovery phase on the log–log plot less fit had been achieved (Fig. 8). Also in the history match of the validation, there is a difference obvious in the draw down phase that is resulting from the practical complexity of the technical pumping test execution that could not be accounted for. Having said this, the numerical model is overall able to reproduce the field behavior, with the

**Table 5 Matrix permeability values are shown below which the flow regime noted to its right is possible**

| spec. matrix storage [1/Pa] | spec. fault storage [1/Pa] | Fault zone thickness [m] | matrix permeability [m²] (radial) | matrix permeability [m²] (bilinear) | matrix permeability [m²] (linear) | matrix as boundary |
|---|---|---|---|---|---|---|
| 2.0 x 10⁻¹² | 1.6 x 10⁻¹⁰ | 15 | $9 \times 10^{-14}$ | $9 \times 10^{-15}$ | $3 \times 10^{-15}$ | |
| | | 35 | $9 \times 10^{-14}$ | $1 \times 10^{-14}$ | $4 \times 10^{-15}$ | |
| | | 50 | $9 \times 10^{-14}$ | $1 \times 10^{-14}$ | $4 \times 10^{-15}$ | |
| | | 100 | $1 \times 10^{-13}$ | $2 \times 10^{-14}$ | $3 \times 10^{-15}$ | |
| | | 150 | $2 \times 10^{-13}$ | $6 \times 10^{-14}$ | $3 \times 10^{-15}$ | |
| | | 200 | $1 \times 10^{-13}$ | $5 \times 10^{-14}$ | $5 \times 10^{-15}$ | |
| | | 300 | $1 \times 10^{-13}$ | $4 \times 10^{-14}$ | $6 \times 10^{-15}$ | |
| | 2.0 x 10⁻¹² | 15 | $4 \times 10^{-14}$ | $3 \times 10^{-15}$ | $1 \times 10^{-16}$ | |
| | | 35 | $4 \times 10^{-14}$ | $3 \times 10^{-15}$ | $2 \times 10^{-16}$ | |
| | | 50 | $3 \times 10^{-14}$ | $3 \times 10^{-15}$ | $3 \times 10^{-16}$ | |
| | | 100 | $4 \times 10^{-14}$ | $3 \times 10^{-15}$ | $4 \times 10^{-16}$ | |
| | | 150 | $5 \times 10^{-14}$ | $6 \times 10^{-15}$ | $6 \times 10^{-16}$ | |
| | | 200 | $4 \times 10^{-14}$ | $3 \times 10^{-15}$ | $7 \times 10^{-16}$ | |
| | | 300 | $3 \times 10^{-14}$ | $3 \times 10^{-15}$ | $9 \times 10^{-16}$ | |
| 1.6 x 10⁻¹⁰ | 1.6 x 10⁻¹⁰ | 15 | $3 \times 10^{-14}$ | $3 \times 10^{-15}$ | $1 \times 10^{-16}$ | |
| | | 35 | $3 \times 10^{-14}$ | $3 \times 10^{-15}$ | $2 \times 10^{-16}$ | |
| | | 50 | $3 \times 10^{-14}$ | $3 \times 10^{-15}$ | $3 \times 10^{-16}$ | |
| | | 100 | $4 \times 10^{-14}$ | $4 \times 10^{-15}$ | $5 \times 10^{-16}$ | |
| | | 150 | $5 \times 10^{-14}$ | $6 \times 10^{-15}$ | $6 \times 10^{-16}$ | |
| | | 200 | $4 \times 10^{-14}$ | $3 \times 10^{-15}$ | $9 \times 10^{-16}$ | |
| | | 300 | $4 \times 10^{-14}$ | $4 \times 10^{-15}$ | $1 \times 10^{-16}$ | |
| | 2.0 x 10⁻¹² | 15 | $3 \times 10^{-14}$ | $8 \times 10^{-16}$ | $3 \times 10^{-17}$ | |
| | | 35 | $3 \times 10^{-14}$ | $9 \times 10^{-16}$ | $5 \times 10^{-17}$ | |
| | | 50 | $3 \times 10^{-14}$ | $9 \times 10^{-16}$ | $6 \times 10^{-17}$ | |
| | | 100 | $4 \times 10^{-14}$ | $1 \times 10^{-15}$ | $1 \times 10^{-16}$ | |
| | | 150 | $5 \times 10^{-14}$ | $2 \times 10^{-15}$ | $1 \times 10^{-16}$ | |
| | | 200 | $4 \times 10^{-14}$ | $1 \times 10^{-15}$ | $1 \times 10^{-16}$ | |
| | | 300 | $4 \times 10^{-14}$ | $1 \times 10^{-15}$ | $1 \times 10^{-16}$ | |

Flow regime labels (left to right): radial | bilinear | linear | matrix as boundary

The table has been derived from the corresponding regression functions for minimum and maximum values of specific fault and matrix storage and for a fault permeability of 1.0e−9 m²

same pressure difference between start and end of the production phase. Also the recovery phase of the pumping test data was reproduced well which can be seen in the middle time region of the log–log plot and in the history matching plot. This confirms the underlying hydrogeological concept and also the realistic nature of the created numerical model.

A great challenge for solving the proposed question is a sufficient sampling over the parameter input space. Since an individual model run takes on average 10 min to finish, it is only possible to carry out an analysis like this by utilizing an HPC cluster. Even though a total number of 30,492 simulations were carried out, an inaccuracy in discovering the flow regime transition depending on the parameter grid resolution remains. The polynomial regression model introduces an additional error for the adjacent interpretation which is also partly based on the amount of simulations as well as on the model type itself. Furthermore, the chosen flow regimes classes are more or less subjective and one could define them differently. However, the focus of this work is on identifying

the parameter space in which a given flow regime is possible. Choosing the classes on which the automated PTA is base differently would mainly just change the intercept of the regression functions, and also by approaching the data evaluation conservative and interpreting the regression functions as limiting surfaces below (lower matrix permeability) which the associated flow type is very likely to be observed, it is still valid to pursue an interpretation as done here.

Needless to say, the presented numerical model is limited by its fundamental assumptions, especially regarding the chosen geometry of well and fault zone. But through the application of characteristic fault zone sizes and a punctual intersection between well and fault zone as it is always the case for geothermal wells in the Malm aquifer, the goal of capturing the basic hydraulic fault zone behavior was reached. Further investigations are now possible by increasing the complexity of additional geometric variables, for example the inclination of fault zone and well. Additionally, future studies could benefit from more high-resolution seismic information and refine the appearance of fault zones into more than one characteristic geometric type.

Besides that, it has to be noted that in the model no well storage and skin effects have been considered as they are present in all hydraulic field data. Also, the simulation time had been chosen way longer than a normal pumping test would last. This makes it possible for some parameter combinations to observe flow types on different timescales than compared to the field. Those two factors mean that more of the fault zone-related flow regimes have been discovered in this analysis than it would be possible in a pumping test. The determined transitions in parameter space should hence be seen as theoretical values portraying flow regimes under ideal conditions. The consequence of this is that there are parameter combinations conceivable that should indicate a fault zone-related flow regime in a pumping test based on the findings of this work, while in reality they can be masked by well effects or remain undetected due to the timescale of the pumping test.

An advantage of using numerical simulations to investigate the flow-type dependency on the parameter space is the possibility to account for the complexity of realistic geometries, meaning an inclined fault and water production over the whole filter length of the well, based on geological and field data and then investigating the actual parameter space of the researched aquifer. A conclusion that the effect of a low conductivity fracture is magnified with higher matrix permeability values found by Heber Cinco et al. (1978) through analytical investigations is in agreement with the observations based on the numerical simulations of realistic aquifer geometries calculated in this work.

Another important point is that the actual parameter range for the Malm aquifer has been identified in which a fault zone with better hydraulic properties compared to the surrounding matrix is present, while only radial behavior is recorded in the pumping tests. Based on this identified range, a quantification of the productivity increase of an exploration site through such a hidden fault is now possible. Birner (2013) shows that the reservoir permeability increases from south to north in the area of Munich. Combining this spatial information with the findings of this work, it can be concluded that an observation of a fault zone in a pumping test is not likely in the city area of Munich but only south of it. To locate this boundary spatially, more data about the aquifers permeability distribution are needed. But this generally fits to the

observation presented at the beginning that only three of 37 wells in this domain portray bilinear or linear flow behavior. It seems likely now that some of these wells tap into productivity improving fault zones that are hidden in their pumping tests, which is a crucial information for the development of future drilling targets.

## Conclusion

The presented investigation illustrates a workflow to explore the transition between different flow regimes associated with fault zones developed through a geothermal well while accounting for realistic geometries and directly scanning a real-world parameter space. A suitable numerical model based on an unstructured tetrahedral mesh has been built. A range of the important hydraulic properties for the Malm aquifer have been gathered. Sampling over this parameter space has been done by calculating the hydraulic response of the aquifer for over 30,000 parameter combinations through deploying the model on an HPC cluster. This resulted in a successful identification of occurring flow regime transitions. These results can be further used to determine reservoir conditions in which the hydraulic behavior around a well is dominated by fault zones. The use of the resulting regression functions allows for a convenient way to investigate individual hydraulic parameters in the planning phase of a geothermal exploration site. Additionally, extreme values for the observation of fault zone-related flow regimes have been identified. This means bilinear flow can only be observed for the Malm aquifer if the matrix permeability is less than $2.0 \times 10^{-13}$ m$^2$. For a matrix permeability less than $6.0 \times 10^{-14}$ m$^2$, linear flow can occur, while negative boundary flow can be detected for values smaller than $6.0 \times 10^{-15}$ m$^2$. Also it was shown that there is an area in parameter space that allows for a fault zone with better hydraulic properties than those of the matrix, while still only radial flow can be observed in the pressure derivative of a pumping test.

**Authors' contributions**
All authors designed this study's workflow and interpreted the results of the parametric analysis. FK carried out the individual steps of the presented workflow. AS was a major contributor in the model calibration and parameter range data. All authors read and approved the final manuscript.

**Author details**
[1] Technical University Munich, Arcisstraße 21, 80333 Munich, Germany. [2] Erdwerk GmbH, Bonner Platz 1, 80803 Munich, Germany. [3] RWTH Aachen University, Schinkelstr. 2, 52062 Aachen, Germany.

# Appendices

## Appendix 1. Regression predictors $x_i$, dependent variable $y$

$x_0 = S_{S,\text{fault}} \times 5 \times 10^8$
$x_1 = \log(K_{\text{fault}})$
$x_2 = S_{S,\text{matrix}} \times 5 \times 10^8$
$x_3 = h_{\text{fault}}$
$y = \log(K_{\text{matrix}})$

$S_S$: specific storage coefficient [1/Pa], $K$: permeability [m²], $h$: thickness [m]

## Appendix 2. Regression scaling

| Transition | $x_0$ | $x_1$ | $x_2$ | $x_3$ |
|---|---|---|---|---|
| Radial to bilinear | | | | |
| Mean | 0.04051 | − 11.49910 | 0.04049 | 102.88885 |
| Standard deviation | 0.02698 | 1.58071 | 0.02698 | 100.21314 |
| Bilinear to linear | | | | |
| Mean | 0.03954 | − 11.19080 | 0.03990 | 102.99182 |
| Standard deviation | 0.02692 | 1.41923 | 0.02714 | 99.20036 |
| Linear to neg. boundary | | | | |
| Mean | 0.04239 | − 11.20684 | 0.03899 | 113.19850 |
| Standard deviation | 0.02658 | 1.48145 | 0.02721 | 102.18529 |

## Appendix 3. Regression functions

Konrad *et al. Geotherm Energy* (2019) 7:25

Page 24 of 28

| Variables of each polynomial term | $1$ | $x_0$ | $x_1$ | $x_2$ | $x_3$ | $x_0^2$ | $x_0 \cdot x_1$ | $x_0 \cdot x_2$ | $x_0 \cdot x_3$ |
|---|---|---|---|---|---|---|---|---|---|
| Coefficient of surface 1 | $-2.01 \times 10^{-15}$ | $3.14 \times 10^{-2}$ | $-3.57 \times 10^{-2}$ | $-2.29 \times 10^{-2}$ | $9.63 \times 10^{-2}$ | $3.89 \times 10^{-2}$ | $-1.16 \times 10^{-3}$ | $-8.34 \times 10^{-3}$ | $3.07 \times 10^{-2}$ |
| Coefficient of surface 2 | $-3.95 \times 10^{-15}$ | $6.91 \times 10^{-2}$ | $1.21 \times 10^{-2}$ | $-1.13 \times 10^{-1}$ | $4.13 \times 10^{-1}$ | $-4.00 \times 10^{-2}$ | $-6.89 \times 10^{-3}$ | $2.12 \times 10^{-2}$ | $-8.16 \times 10^{-2}$ |
| Coefficient of surface 3 | $4.84 \times 10^{-16}$ | $2.15 \times 10^{-1}$ | $1.45 \times 10^{-1}$ | $-2.81 \times 10^{-1}$ | $1.20 \times 10^{-1}$ | $-5.02 \times 10^{-2}$ | $-2.40 \times 10^{-2}$ | $4.57 \times 10^{-2}$ | $-5.98 \times 10^{-2}$ |

| | $x_0 \cdot x_1^2$ | $x_0 \cdot x_1 \cdot x_2$ | $x_0 \cdot x_1 \cdot x_3$ | $x_0 \cdot x_2^2$ | $x_0 \cdot x_2 \cdot x_3$ | $x_0 \cdot x_3^2$ | $x_1^3$ | $x_1^2 \cdot x_2$ | $x_1^2 \cdot x_3$ |
|---|---|---|---|---|---|---|---|---|---|
| Surface 1 | $3.65 \times 10^{-2}$ | $-1.51 \times 10^{-4}$ | $-3.69 \times 10^{-2}$ | $1.77 \times 10^{-2}$ | $-2.63 \times 10^{-2}$ | $-2.60 \times 10^{-2}$ | $3.57 \times 10^{-3}$ | $2.00 \times 10^{-1}$ | $-8.58 \times 10^{-3}$ |
| Surface 2 | $3.80 \times 10^{-2}$ | $2.23 \times 10^{-2}$ | $-2.81 \times 10^{-2}$ | $2.55 \times 10^{-2}$ | $4.39 \times 10^{-3}$ | $-9.66 \times 10^{-2}$ | $5.50 \times 10^{-2}$ | $1.66 \times 10^{-1}$ | $-1.06 \times 10^{-2}$ |
| Surface 3 | $7.03 \times 10^{-2}$ | $-0.94 \times 10^{-2}$ | $5.89 \times 10^{-3}$ | $-3.29 \times 10^{-2}$ | $-7.99 \times 10^{-2}$ | $3.25 \times 10^{-2}$ | $4.33 \times 10^{-2}$ | $7.54 \times 10^{-2}$ | $0.56 \times 10^{-1}$ |

| | $x_0^3 \cdot x_1$ | $x_0^3 \cdot x_2$ | $x_0^3 \cdot x_3$ | $x_0^2 \cdot x_1^2$ | $x_0^2 \cdot x_1 \cdot x_2$ | $x_0^2 \cdot x_1 \cdot x_3$ | $x_0^2 \cdot x_2^2$ | $x_0^2 \cdot x_2 \cdot x_3$ | $x_0^2 \cdot x_3^2$ |
|---|---|---|---|---|---|---|---|---|---|
| Surface 1 | $9.98 \times 10^{-4}$ | $-1.42 \times 10^{-2}$ | $3.52 \times 10^{-3}$ | $-1.02 \times 10^{-2}$ | $5.21 \times 10^{-3}$ | $5.88 \times 10^{-3}$ | $-2.98 \times 10^{-2}$ | $3.60 \times 10^{-3}$ | $0.24 \times 10^{-2}$ |
| Surface 2 | $7.86 \times 10^{-3}$ | $-3.32 \times 10^{-2}$ | $4.97 \times 10^{-2}$ | $-5.94 \times 10^{-3}$ | $-4.54 \times 10^{-3}$ | $-5.90 \times 10^{-4}$ | $-3.08 \times 10^{-3}$ | $-3.37 \times 10^{-2}$ | $3.78 \times 10^{-2}$ |
| Surface 3 | $1.08 \times 10^{-2}$ | $-3.80 \times 10^{-2}$ | $2.47 \times 10^{-2}$ | $-2.47 \times 10^{-3}$ | $1.67 \times 10^{-3}$ | $1.79 \times 10^{-2}$ | $-4.57 \times 10^{-3}$ | $-1.88 \times 10^{-2}$ | $7.72 \times 10^{-3}$ |

| | $x_0 \cdot x_3^3$ | $x_1^4$ | $x_1^3 \cdot x_2$ | $x_1^3 \cdot x_3$ | $x_1^2 \cdot x_2^2$ | $x_1^2 \cdot x_2 \cdot x_3$ | $x_1^2 \cdot x_3^2$ | $x_1 \cdot x_3^2$ | $x_1 \cdot x_2^2 \cdot x_3$ |
|---|---|---|---|---|---|---|---|---|---|
| Surface 1 | $-1.98 \times 10^{-2}$ | $-2.40 \times 10^{-2}$ | $3.56 \times 10^{-2}$ | $-2.85 \times 10^{-2}$ | $8.93 \times 10^{-3}$ | $3.99 \times 10^{-2}$ | $-2.24 \times 10^{-1}$ | $1.74 \times 10^{-2}$ | $1.88 \times 10^{-3}$ |
| Surface 2 | $3.01 \times 10^{-2}$ | $-1.74 \times 10^{-2}$ | $1.86 \times 10^{-2}$ | $-9.72 \times 10^{-3}$ | $1.70 \times 10^{-2}$ | $2.76 \times 10^{-3}$ | $-1.26 \times 10^{-1}$ | $-7.30 \times 10^{-3}$ | $8.53 \times 10^{-3}$ |
| Surface 3 | $4.82 \times 10^{-2}$ | $2.28 \times 10^{-2}$ | $-6.81 \times 10^{-3}$ | $1.64 \times 10^{-2}$ | $-8.23 \times 10^{-3}$ | $-4.39 \times 10^{-3}$ | $8.96 \times 10^{-3}$ | $-6.79 \times 10^{-3}$ | $-1.67 \times 10^{-2}$ |

| | $x_0^4 \cdot x_2$ | $x_0^4 \cdot x_3$ | $x_0^3 \cdot x_1^2$ | $x_0^3 \cdot x_1 \cdot x_2$ | $x_0^3 \cdot x_1 \cdot x_3$ | $x_0^3 \cdot x_2^2$ | $x_0^3 \cdot x_2 \cdot x_3$ | $x_0^3 \cdot x_3^2$ | $x_0^2 \cdot x_1^3$ |
|---|---|---|---|---|---|---|---|---|---|
| Surface 1 | $1.04 \times 10^{-2}$ | $7.92 \times 10^{-4}$ | $4.86 \times 10^{-3}$ | $-6.24 \times 10^{-3}$ | $-4.21 \times 10^{-3}$ | $2.07 \times 10^{-2}$ | $-1.31 \times 10^{-3}$ | $-2.32 \times 10^{-3}$ | $7.11 \times 10^{-3}$ |
| Surface 2 | $2.16 \times 10^{-2}$ | $-1.90 \times 10^{-2}$ | $1.82 \times 10^{-3}$ | $7.73 \times 10^{-4}$ | $2.62 \times 10^{-3}$ | $5.57 \times 10^{-3}$ | $2.32 \times 10^{-2}$ | $-2.44 \times 10^{-2}$ | $3.83 \times 10^{-3}$ |
| Surface 3 | $3.36 \times 10^{-2}$ | $-1.31 \times 10^{-2}$ | $-1.05 \times 10^{-2}$ | $-4.77 \times 10^{-3}$ | $7.02 \times 10^{-3}$ | $2.61 \times 10^{-2}$ | $1.01 \times 10^{-2}$ | $-7.13 \times 10^{-3}$ | $8.56 \times 10^{-3}$ |

| | $x_0 \cdot x_1^4$ | $x_0 \cdot x_1^3 \cdot x_2$ | $x_0 \cdot x_1^3 \cdot x_3$ | $x_0 \cdot x_1^2 \cdot x_2^2$ | $x_0 \cdot x_1^2 \cdot x_2 \cdot x_3$ | $x_0 \cdot x_1^2 \cdot x_3^2$ | $x_0 \cdot x_1 \cdot x_3^2$ | $x_0 \cdot x_1 \cdot x_2 \cdot x_3^2$ | $x_0 \cdot x_1 \cdot x_2^2 \cdot x_3$ |
|---|---|---|---|---|---|---|---|---|---|
| Surface 1 | $-8.23 \times 10^{-3}$ | $1.47 \times 10^{-3}$ | $2.74 \times 10^{-3}$ | $-6.92 \times 10^{-4}$ | $5.60 \times 10^{-3}$ | $-8.51 \times 10^{-3}$ | $1.65 \times 10^{-2}$ | $-7.76 \times 10^{-3}$ | $8.92 \times 10^{-3}$ |
| Surface 2 | $-1.07 \times 10^{-2}$ | $8.15 \times 10^{-3}$ | $-6.17 \times 10^{-3}$ | $1.50 \times 10^{-3}$ | $-2.13 \times 10^{-3}$ | $-6.06 \times 10^{-3}$ | $2.70 \times 10^{-3}$ | $-1.85 \times 10^{-3}$ | $1.47 \times 10^{-2}$ |
| Surface 3 | $-1.73 \times 10^{-2}$ | $7.51 \times 10^{-3}$ | $3.81 \times 10^{-3}$ | $1.34 \times 10^{-2}$ | $-6.21 \times 10^{-3}$ | $-9.50 \times 10^{-3}$ | $2.84 \times 10^{-3}$ | $5.60 \times 10^{-4}$ | $-5.04 \times 10^{-3}$ |

Konrad *et al. Geotherm Energy* (2019) 7:25

Page 25 of 28

| Term | Value 1 | Value 2 | Value 3 |
|---|---|---|---|
| $x_1^3 \cdot x_2^2$ | $-0.13 \times 10^{-1}$ | $-1.13 \times 10^{-2}$ | $1.12 \times 10^{-3}$ |
| $x_1^3 \cdot x_2 \cdot x_3$ | $-1.12 \times 10^{-2}$ | $3.82 \times 10^{-3}$ | $-2.15 \times 10^{-3}$ |
| $x_1^3 \cdot x_3^2$ | $2.54 \times 10^{-2}$ | $-5.94 \times 10^{-3}$ | $-2.01 \times 10^{-2}$ |
| $x_1^2 \cdot x_2^3$ | $-3.29 \times 10^{-3}$ | $-3.16 \times 10^{-5}$ | $4.13 \times 10^{-3}$ |
| $x_1^2 \cdot x_2^2 \cdot x_3$ | $-2.08 \times 10^{-2}$ | $-7.07 \times 10^{-4}$ | $4.55 \times 10^{-3}$ |
| $x_1^2 \cdot x_2 \cdot x_3^2$ | $-2.45 \times 10^{-2}$ | $-4.17 \times 10^{-3}$ | $-3.61 \times 10^{-3}$ |
| $x_1^2 \cdot x_3^3$ | $8.24 \times 10^{-2}$ | $4.26 \times 10^{-2}$ | $-1.57 \times 10^{-2}$ |
| $x_1 \cdot x_2^4$ | $-7.97 \times 10^{-3}$ | $8.32 \times 10^{-3}$ | $7.45 \times 10^{-3}$ |
| $x_1 \cdot x_2^3 \cdot x_3$ | $1.84 \times 10^{-2}$ | $3.71 \times 10^{-3}$ | $-4.22 \times 10^{-3}$ |
| $x_1^2$ | $-1.17 \times 10^{-1}$ | $-1.20 \times 10^{-1}$ | $-1.93 \times 10^{-1}$ |
| $x_1 \cdot x_2$ | $-9.83 \times 10^{-2}$ | $6.59 \times 10^{-3}$ | $3.24 \times 10^{-2}$ |
| $x_1 \cdot x_3$ | $1.39 \times 10^{-1}$ | $3.22 \times 10^{-2}$ | $-9.00 \times 10^{-2}$ |
| $x_2^2$ | $4.15 \times 10^{-2}$ | $-6.13 \times 10^{-3}$ | $-1.58 \times 10^{-2}$ |
| $x_2 \cdot x_3$ | $-1.39 \times 10^{-1}$ | $-3.97 \times 10^{-2}$ | $3.10 \times 10^{-2}$ |
| $x_3^2$ | $4.18 \times 10^{-1}$ | $4.83 \times 10^{-1}$ | $-1.14 \times 10^{-1}$ |
| $x_3^3$ | $-1.92 \times 10^{-2}$ | $2.40 \times 10^{-2}$ | $-2.21 \times 10^{-2}$ |
| $x_0^2 \cdot x_1$ | $-2.27 \times 10^{-3}$ | $-6.70 \times 10^{-3}$ | $-2.04 \times 10^{-2}$ |
| $x_0^2 \cdot x_2$ | $-4.83 \times 10^{-2}$ | $-3.50 \times 10^{-2}$ | $-2.20 \times 10^{-2}$ |
| $x_1^2 \cdot x_3$ | $1.95 \times 10^{-1}$ | $1.27 \times 10^{-1}$ | $1.63 \times 10^{-1}$ |
| $x_1 \cdot x_2^2$ | $5.31 \times 10^{-2}$ | $1.98 \times 10^{-3}$ | $-4.35 \times 10^{-2}$ |
| $x_1 \cdot x_2 \cdot x_3$ | $-3.84 \times 10^{-2}$ | $-4.50 \times 10^{-2}$ | $4.26 \times 10^{-2}$ |
| $x_1 \cdot x_3^2$ | $1.50 \times 10^{-1}$ | $1.59 \times 10^{-1}$ | $8.15 \times 10^{-2}$ |
| $x_2^3$ | $-9.66 \times 10^{-3}$ | $3.51 \times 10^{-2}$ | $3.37 \times 10^{-2}$ |
| $x_2^2 \cdot x_3$ | $3.43 \times 10^{-2}$ | $2.38 \times 10^{-2}$ | $-7.35 \times 10^{-2}$ |
| $x_2 \cdot x_3^2$ | $3.19 \times 10^{-2}$ | $-3.86 \times 10^{-2}$ | $2.68 \times 10^{-2}$ |
| $x_3^3$ | $-2.19 \times 10^{-1}$ | $-5.23 \times 10^{-1}$ | $3.57 \times 10^{-1}$ |
| $x_0^4$ | $-8.30 \times 10^{-3}$ | $-2.85 \times 10^{-2}$ | $-1.84 \times 10^{-2}$ |
| $x_0 \cdot x_1^3$ | $-3.59 \times 10^{-3}$ | $-7.26 \times 10^{-3}$ | $-6.52 \times 10^{-3}$ |
| $x_0 \cdot x_1^2 \cdot x_2$ | $2.89 \times 10^{-3}$ | $-4.19 \times 10^{-3}$ | $-9.84 \times 10^{-3}$ |
| $x_0 \cdot x_1^2 \cdot x_3$ | $1.12 \times 10^{-2}$ | $9.48 \times 10^{-3}$ | $3.25 \times 10^{-2}$ |
| $x_0 \cdot x_1 \cdot x_2^2$ | $-1.12 \times 10^{-2}$ | $-5.32 \times 10^{-3}$ | $-9.16 \times 10^{-3}$ |
| $x_0 \cdot x_1 \cdot x_2 \cdot x_3$ | $-2.30 \times 10^{-2}$ | $-3.76 \times 10^{-2}$ | $4.80 \times 10^{-3}$ |
| $x_0 \cdot x_1 \cdot x_3^2$ | $7.44 \times 10^{-3}$ | $3.86 \times 10^{-2}$ | $3.17 \times 10^{-2}$ |
| $x_0 \cdot x_2^3$ | $-9.02 \times 10^{-3}$ | $1.22 \times 10^{-2}$ | $1.87 \times 10^{-2}$ |
| $x_0 \cdot x_2^2 \cdot x_3$ | $-1.10 \times 10^{-2}$ | $8.96 \times 10^{-4}$ | $-4.06 \times 10^{-2}$ |
| $x_0 \cdot x_2 \cdot x_3^2$ | $1.35 \times 10^{-2}$ | $-2.46 \times 10^{-2}$ | $-2.07 \times 10^{-2}$ |
| $x_1 \cdot x_2 \cdot x_3^2$ | $5.36 \times 10^{-2}$ | $4.01 \times 10^{-3}$ | $-3.91 \times 10^{-2}$ |
| $x_1 \cdot x_3^3$ | $-4.45 \times 10^{-1}$ | $-3.17 \times 10^{-1}$ | $-7.61 \times 10^{-2}$ |
| $x_2^4$ | $3.39 \times 10^{-2}$ | $5.32 \times 10^{-2}$ | $8.89 \times 10^{-2}$ |
| $x_2^3 \cdot x_3$ | $2.98 \times 10^{-2}$ | $2.54 \times 10^{-2}$ | $3.53 \times 10^{-2}$ |
| $x_2^2 \cdot x_3^2$ | $-2.06 \times 10^{-2}$ | $8.17 \times 10^{-3}$ | $4.22 \times 10^{-2}$ |
| $x_2 \cdot x_3^3$ | $5.15 \times 10^{-2}$ | $5.67 \times 10^{-2}$ | $-1.77 \times 10^{-2}$ |
| $x_3^4$ | $-5.48 \times 10^{-1}$ | $-8.23 \times 10^{-1}$ | $-2.72 \times 10^{-1}$ |
| $x_3^5$ | $2.53 \times 10^{-3}$ | $1.51 \times 10^{-2}$ | $2.24 \times 10^{-2}$ |
| $x_0^4 \cdot x_1$ | $1.79 \times 10^{-3}$ | $-3.20 \times 10^{-3}$ | $-5.14 \times 10^{-3}$ |
| $x_0^2 \cdot x_1 \cdot x_2$ | $8.25 \times 10^{-4}$ | $-1.50 \times 10^{-3}$ | $-9.10 \times 10^{-3}$ |
| $x_0^2 \cdot x_1 \cdot x_3$ | $-2.79 \times 10^{-3}$ | $4.34 \times 10^{-3}$ | $-1.07 \times 10^{-2}$ |
| $x_0^2 \cdot x_1 \cdot x_3^2$ | $1.63 \times 10^{-3}$ | $2.15 \times 10^{-3}$ | $-1.00 \times 10^{-2}$ |
| $x_0^2 \cdot x_2^2$ | $-2.25 \times 10^{-4}$ | $5.18 \times 10^{-4}$ | $-6.16 \times 10^{-3}$ |
| $x_0^2 \cdot x_2^3$ | $2.66 \times 10^{-2}$ | $4.79 \times 10^{-4}$ | $-6.51 \times 10^{-3}$ |
| $x_0^2 \cdot x_2 \cdot x_3^2$ | $-2.30 \times 10^{-3}$ | $-4.29 \times 10^{-3}$ | $3.81 \times 10^{-2}$ |
| $x_0^2 \cdot x_2^2 \cdot x_3$ | $2.53 \times 10^{-3}$ | $2.05 \times 10^{-2}$ | $1.07 \times 10^{-2}$ |
| $x_0^2 \cdot x_3^3$ | $-1.26 \times 10^{-3}$ | $-1.68 \times 10^{-2}$ | $-2.84 \times 10^{-3}$ |

| $x_0 \cdot x_1 \cdot x_3^3$ | $x_0 \cdot x_2^4$ | $x_0 \cdot x_2^3 \cdot x_3$ | $x_0 \cdot x_2^2 \cdot x_3^2$ | $x_0 \cdot x_2 \cdot x_3^3$ | $x_0 \cdot x_3^4$ | $x_1^5$ | $x_1^4 \cdot x_2$ | $x_1^4 \cdot x_3$ |
|---|---|---|---|---|---|---|---|---|
| $-2.25 \times 10^{-3}$ | $9.23 \times 10^{-3}$ | $1.70 \times 10^{-2}$ | $-4.00 \times 10^{-3}$ | $-7.91 \times 10^{-3}$ | $9.93 \times 10^{-3}$ | $-2.17 \times 10^{-2}$ | $-5.63 \times 10^{-3}$ | $-3.25 \times 10^{-2}$ |
| $-1.99 \times 10^{-2}$ | $-5.05 \times 10^{-3}$ | $1.87 \times 10^{-2}$ | $-8.15 \times 10^{-3}$ | $1.44 \times 10^{-2}$ | $-1.36 \times 10^{-2}$ | $-1.67 \times 10^{-2}$ | $-3.71 \times 10^{-3}$ | $-1.71 \times 10^{-2}$ |
| $-1.72 \times 10^{-2}$ | $-9.37 \times 10^{-3}$ | $-2.48 \times 10^{-3}$ | $2.32 \times 10^{-2}$ | $5.41 \times 10^{-3}$ | $-3.18 \times 10^{-2}$ | $-1.04 \times 10^{-2}$ | $-1.45 \times 10^{-2}$ | $-3.10 \times 10^{-2}$ |

| $x_1 \cdot x_2^2 \cdot x_3^2$ | $x_1 \cdot x_2 \cdot x_3^3$ | $x_1 \cdot x_3^4$ | $x_2^5$ | $x_2^4 \cdot x_3$ | $x_2^3 \cdot x_3^2$ | $x_2^2 \cdot x_3^3$ | $x_2 \cdot x_3^4$ | $x_3^5$ |
|---|---|---|---|---|---|---|---|---|
| $-7.88 \times 10^{-3}$ | $-1.79 \times 10^{-2}$ | $1.68 \times 10^{-1}$ | $-2.53 \times 10^{-2}$ | $-1.14 \times 10^{-2}$ | $-6.35 \times 10^{-3}$ | $1.07 \times 10^{-2}$ | $-2.21 \times 10^{-2}$ | $2.74 \times 10^{-1}$ |
| $-7.36 \times 10^{-3}$ | $2.32 \times 10^{-3}$ | $1.19 \times 10^{-1}$ | $-4.03 \times 10^{-2}$ | $-7.08 \times 10^{-3}$ | $-7.53 \times 10^{-3}$ | $-5.05 \times 10^{-3}$ | $-1.88 \times 10^{-2}$ | $4.61 \times 10^{-1}$ |
| $1.62 \times 10^{-2}$ | $1.12 \times 10^{-2}$ | $2.52 \times 10^{-2}$ | $-4.93 \times 10^{-2}$ | $-7.10 \times 10^{-3}$ | $-3.65 \times 10^{-2}$ | $-1.25 \times 10^{-2}$ | $1.07 \times 10^{-2}$ | $5.93 \times 10^{-2}$ |

| | |
|---|---|
| Intercept of surface 1 | $-1.35 \times 10^1$ |
| Intercept of surface 2 | $-1.45 \times 10^1$ |
| Intercept of surface 3 | $-1.53 \times 10^1$ |

Surface 1: boundary surface between radial and bilinear flows; surface 2: boundary surface between bilinear and linear flows; surface 3: boundary surface between linear and boundary flows

Konrad *et al. Geotherm Energy*     (2019) 7:25

Page 27 of 28

### References

Agemar T, Alten J, Ganz B, Kuder J, Kühne K, Schumacher S, Schulz R. The geothermal information system for Germany—GeotIS, Zeitschrift der Dtsch. Gesellschaft für Geowissenschaften. 2014;165:129–44. https://doi.org/10.1127/1860-1804/2014/0060.

Agosta F, Aydin A. Architecture and deformation mechanism of a basin-bounding normal fault in Mesozoic platform carbonates, central Italy. J Struct Geol. 2006;28:1445–67. https://doi.org/10.1016/j.jsg.2006.04.006.

Ahrens J, Geveci B, Law C. ParaView: an end-user tool for large data visualization, visualization handbook. New York: Elsevier; 2005.

Alfonsi A, Rabiti C, Mandelli D, Cogliati J, Wang C, Talbot PW, Maljovec DP, Smith C. RAVEN theory manual and user guide. Idaho: Idaho National Laboratory; 2017.

Alt W, Kahnt R. Hydraulische Untersuchungen. In: Bauer M, Freeden W, Jacobi H, Neu T, editors. Handbuch tiefe geothermie. Berlin: Springer; 2014. p. 609–58.

Bachmann GH, Dohr G, Müller M. Exploration in a classic thrust belt and its foreland Bavarian Alps, Germany. Am Assoc Pet Geol Bull. 1982;66:2529–42.

Bachmann GH, Müller M, Weggen K. Evolution of the Molasse Basin (Germany, Switzerland). Tectonophysics. 1987;137:77–92. https://doi.org/10.1016/0040-1951(87)90315-5.

Bear J. Dynamics of fluids in porous media. New York: Dover; 1972.

Birner J. Hydrogeologisches Modell des Malmaquifers im Süddeutschen Molassebecken. Berlin: Freie University; 2013.

Blöcher G, Cacace M, Blöcher G, Cacace M. MeshIt—a software for three dimensional volumetric meshing of complex faulted reservoirs. Comput Geosci. 2015;74:5191–209. https://doi.org/10.1007/s12665-015-4537-x.

Böhm F, Savvatis A, Steiner U. Innovative Explorationsstrategie. In: Verbundvorhaben: Wissenschaftliche Und Technische Grundlagen Zur Strukturgeologischen Und Hydrogeologischen Charakterisierung Tiefer Geothermisch Genutzter Grundwasserleiter Am Beispiel Des Süddeutschen Molassebeckens. 2012. p. 129–54.

Böhm F, Savvatis A, Steiner U, Schneider M, Koch R. Lithofazielle Reservoircharakterisierung zur geothermischen Nutzung des Malm im Großraum München. Grundwasser. 2013;18:3–13. https://doi.org/10.1007/s00767-012-0202-4.

Bourdet D. Well test analysis : the use of advanced interpretation models. New York: Elsevier; 2002. https://doi.org/10.1017/CBO9781107415324.004.

Bourdet D, Ayoub JA, Pirard YM. Use of pressure derivative in well test interpretation. SPE Form Eval. 1989. https://doi.org/10.2118/12777-PA.

Bourdet D, Whittle T, Douglas A, Pirard Y. A new set of type cuves simplifies well test analysis. World Oil. 1983. https://doi.org/10.2118/16812-PA.

Buitinck L, Louppe G, Blondel M, Pedregosa F, Mueller A, Grisel O, Niculae V, Prettenhofer P, Gramfort A, Grobler J, Layton, R, Vanderplas J, Joly A, Holt B, Varoquaux G. API design for machine learning software: experiences from the scikit-learn project. 2013. p. 1–15.

Bundschuh J, Suárez Arriaga MC. Introduction to the numerical modeling of groundwater and geothermal systems: fundamentals of mass, energy and solute transport in poroelastic rocks. 2010.

Cacace M, Blöcher G, Watanabe N, Moeck I, Börsing N, Scheck-Wenderoth M, Kolditz O, Huenges E. Modelling of fractured carbonate reservoirs: outline of a novel technique via a case study from the Molasse Basin, southern Bavaria, Germany. Environ Earth Sci. 2013;70:3585–602. https://doi.org/10.1007/s12665-013-2402-3.

Cacace M, Jacquey AB. Flexible parallel implicit modelling of coupled thermal-hydraulic-mechanical processes in fractured rocks. Solid Earth. 2017a;8:921–41. https://doi.org/10.5194/se-8-921-2017.

Cacace M, Jacquey AB. Flexible parallel implicit modelling of coupled thermal-hydraulic-mechanical processes in fractured rocks. Solid Earth. 2017b. https://doi.org/10.5194/se-2017-33.

Caine JS, Evans JP, Forster CB. Fault zone architecture and permeability structure. Geology. 1996;24:1025–8. https://doi.org/10.1130/0091-7613(1996)024%3c1025.

Draper NR, Smith H. Applied regression analysis, 3rd ed. 1998.

Fritzer T. Bayerischer geothermieatlas—hydrothermale energiegewinnung. Infrastruktur, Verkehr und Technologie: Bayerisches Staatsministerium für Wirtschaft; 2012.

Gaston D, Newman C, Hansen G, Lebrun-grandié D. MOOSE: A parallel computational framework for coupled systems of nonlinear equations, in: International Conference on Mathematics, Computational Methods & Reactor Physics (M&C 2009). 2009. p. 1768–78. https://doi.org/10.1016/j.nucengdes.2009.05.021.

Gringarten AC. From straight lines to deconvolution: the evolution of the state of the art in well test analysis. SPE Reserv Eval Eng. 2008;11:18. https://doi.org/10.2118/102079-PA.

Heber Cinco L, Samaniego V, Dominguez A. Transient pressure behavior for a well with a finite-conductivity vertical fracture. Soc Pet Eng J. 1978. https://doi.org/10.2118/6014-PA.

Houze O, Viturat D, Fjaere OS. Dynamic data analysis (DDA). 2017. https://doi.org/10.1007/978-1-4939-7190-9.

Idaho National Laboratory. mooseframework.org: IterationAdaptiveDT [WWW Document]. 2019. https://www.mooseframework.org/source/timesteppers/IterationAdaptiveDT.html#iterationadaptivedt. Accessed 4 Mar 2019.

IHS. iHS Fekete [WWW Document]. 2016. http://www.fekete.ca/. Accessed 28 June 2019.

Leibniz-Rechenzentrum. Leibniz Supercomputing Centre [WWW Document]. 2017. https://www.lrz.de/services/compute/. Accessed 23 Apr 2019.

Lemmon EW, McLinden MO, Friend DG. Thermophysical properties of fluid systems. In: Linstrom PJ, Mallard WG, eds. NIST Chemistry WebBook, NIST Standard Reference Database Number 69. National Institute of Standards and Technology, Gaithersburg; 2018. https://doi.org/10.18434/T4D303.

Lüschen E, Wolfgramm M, Fritzer T, Dussel M, Thomas R, Schulz R. 3D seismic survey explores geothermal targets for reservoir characterization at Unterhaching, Munich, Germany. Geothermics. 2014;50:167–79. https://doi.org/10.1016/j.geothermics.2013.09.007.

Micarelli L, Benedicto A, Wibberley CAJ. Structural evolution and permeability of normal fault zones in highly porous carbonate rocks. J Struct Geol. 2006;28:1214–27. https://doi.org/10.1016/j.jsg.2006.03.036.

Michie EAH, Haines TJ, Healy D, Neilson JE, Timms NE, Wibberley CAJ. Influence of carbonate facies on fault zone architecture. J Struct Geol. 2014;65:82–99. https://doi.org/10.1016/j.jsg.2014.04.007.

Moeck IS, Uhlig S, Loske B, Jentsch A, Mählmann RF, Ferreiro-Maehlmann R, Hild S. Fossil multiphase normal faults—prime targets for geothermal drilling in the bavarian Molasse basin? World Geotherm Congr. 2015;2015:19–25.

Mraz E. Reservoir characterization to improve exploration concepts of the upper jurassic in the southern bavarian Molasse Basin. Munich: Technical University Munich; 2019.

Pedregosa F, Weiss R, Brucher M. Scikit-learn: Machine Learning in Python. 2011; 12: 2825–30.

Petropoulos GP, Srivastava PK. Sensitivity analysis in earth observation modelling. Amsterdam: Elsevier; 2017.

Quenstedt FA. Der Jura. Tübingen: Laupp; 1858.

Savvatis A. Hydraulik. In: Schneider M, Thomas L, eds. Verbundvorhaben: Wissenschaftliche Und Technische Grundlagen Zur Strukturgeologischen Und Hydrogeologischen Charakterisierung Tiefer Geothermisch Genutzter Grundwasserleiter Am Beispiel Des Süddeutschen Molassebeckens. 2012. p. 129–54.

Schneider M, Thomas L. Verbundvorhaben: Wissenschaftliche und technische Grundlagen zur strukturgeologischen und hydrogeologischen Charakterisierung tiefer geothermisch genutzter Grundwasserleiter am Beispiel des süddeutschen Molassebeckens. Endbericht–BMU Forschungsvorhaben. 2012. p. 237.

Scikit-learn user guide: preprocessing data [WWW Document]. 2018. https://scikit-learn.org/stable/modules/preprocessing.html. Accessed 4 Mar 2019.

Steiner U, Böhm F, Savvatis A. Hydrogeologisches Modell. In: Schneider, M., Thomas, L. (Eds.), Verbundvorhaben: Wissenschaftliche Und Technische Grundlagen Zur Strukturgeologischen Und Hydrogeologischen Charakterisierung Tiefer Geothermisch Genutzter Grundwasserleiter Am Beispiel Des Süddeutschen Molassebeckens. 2012. p. 196–220.

Stier P, Prestel R. Der Malmkarst im Süddeutschen Molassebecken—Ein hydrogeologischer Überblick, in: Hydrogeothermische Energiebilanz Und Grundwasserhaushalt Des Malmkarstes Im Süddeutschen Molassebecken (Schlussbericht-Forschungsvorhaben 03 E 6240 A/B). Bay. L.-Amt Wasserwirtschaft & geol. L.-Amt Baden-Württemberg, München, Freiburg. 1991. p. 12.

TUM. Geothermal-Alliance Bavaria [WWW Document]. 2019. https://www.mse.tum.de/gab/. Accessed 23 Apr 2019.

von Hartmann H, Tanner DC, Schumacher S. Initiation and development of normal faults within the German alpine foreland basin: the inconspicuous role of basement structures. Tectonics. 2016;35:1560–74. https://doi.org/10.1002/2016TC004176.

Wolfgramm M, Bartels J, Hoffmann F, Kittl G, Lenz G, Seibt P, Schulz R, Thomas R, Unger HJ, Gmbh GN. Unterhaching geothermal well doublet: structural and hydrodynamic reservoir characteristic. In: Proceedings European Geothermal Congress. Bavaria. 2007.

## Publisher's Note